

Global Biogeochemical Cycles^{*}



RESEARCH ARTICLE

10.1029/2023GB008010

The Modeled Seasonal Cycles of Surface N₂O Fluxes and Atmospheric N₂O

Key Points:

- Model land biosphere and ocean surface fluxes are combined with tropospheric transport to simulate N₂O seasonality at eight monitoring sites
- Surface N₂O fluxes contribute substantially to the observed seasonality of tropospheric N₂O, partly offsetting stratospheric contribution
- Large spread in seasonal land fluxes calls for biosphere model improvements, for example, using N₂O observations and transport-chemistry modeling

Supporting Information:

Supporting Information may be found in the online version of this article.

Correspondence to:

Q. Sun,
qing.sun@unibe.ch

Citation:

Sun, Q., Joos, F., Lienert, S., Berthet, S., Carroll, D., Gong, C., et al. (2024). The modeled seasonal cycles of surface N₂O fluxes and atmospheric N₂O. *Global Biogeochemical Cycles*, 38, e2023GB008010. <https://doi.org/10.1029/2023GB008010>

Received 19 OCT 2023

Accepted 18 JUN 2024

Author Contributions:

Conceptualization: Qing Sun, Fortunat Joos

Data curation: Qing Sun, Sebastian Lienert, Sarah Berthet, Dustin Carroll, Cheng Gong, Akihiko Ito, Atul K. Jain, Sian Kou-Giesbrecht, Angela Landolfi, Manfredi Manizza, Naiqing Pan, Pierre Regnier, Laure Resplandy, Roland Séférian, Hao Shi, Parvatha Suntharalingam, Rona L. Thompson, Hanqin Tian, Nicolas Vuichard, Sönke Zaehle, Qing Zhu











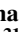








Formal analysis: Qing Sun

Funding acquisition: Fortunat Joos

Investigation: Qing Sun, Fortunat Joos

© 2024 The Author(s).

This is an open access article under the terms of the [Creative Commons Attribution-NonCommercial License](https://creativecommons.org/licenses/by-nc/4.0/), which permits use, distribution and reproduction in any medium, provided the original work is properly cited and is not used for commercial purposes.

Qing Sun^{1,2} , Fortunat Joos^{1,2} , Sebastian Lienert^{1,2} , Sarah Berthet³ , Dustin Carroll⁴ , Cheng Gong⁵, Akihiko Ito^{6,7} , Atul K. Jain⁸ , Sian Kou-Giesbrecht^{9,10} , Angela Landolfi¹¹, Manfredi Manizza¹² , Naiqing Pan^{13,14} , Michael Prather¹⁵ , Pierre Regnier¹⁶, Laure Resplandy¹⁷ , Roland Séférian³ , Hao Shi¹⁸, Parvatha Suntharalingam¹⁹ , Rona L. Thompson²⁰ , Hanqin Tian^{13,14} , Nicolas Vuichard²¹ , Sönke Zaehle⁵ , and Qing Zhu²² 

¹Climate and Environmental Physics, Physics Institute, University of Bern, Bern, Switzerland, ²Oeschger Centre for Climate Change Research, University of Bern, Bern, Switzerland, ³CNRM, Université de Toulouse, Météo France, CNRS, Toulouse, France, ⁴Moss Landing Marine Laboratories, San José State University, Moss Landing, CA, USA, ⁵Biogeochemical Signals Department, Max Planck Institute for Biogeochemistry, Jena, Germany, ⁶Graduate School of Life and Agricultural Sciences, University of Tokyo, Tokyo, Japan, ⁷Earth System Division, National Institute for Environmental Studies, Tsukuba, Japan, ⁸Department of Atmospheric Sciences, University of Illinois, Urbana, IL, USA, ⁹Department of Earth and Environmental Sciences, Dalhousie University, Halifax, NS, Canada, ¹⁰Canadian Centre for Climate Modelling and Analysis, Environment and Climate Change Canada, Victoria, BC, Canada, ¹¹National Research Council, Institute of Marine Sciences (ISMAR-CNR- ISMAR), Rome, Italy, ¹²Geosciences Research Division, Scripps Institution of Oceanography, University of California- San Diego, La Jolla, CA, USA, ¹³Department of Earth and Environmental Sciences, Schiller Institute for Integrated Science and Society, Boston College, Chestnut Hill, MA, USA, ¹⁴International Center for Climate and Global Change Research, College of Forestry, Wildlife and Environment, Auburn University, Auburn, AL, USA, ¹⁵Department of Earth System Science, University of California Irvine, Irvine, CA, USA, ¹⁶Department Geoscience, Environment & Society - BGEOSYS, Université Libre de Bruxelles, Brussels, Belgium, ¹⁷Geosciences Department, Princeton University, High Meadows Environmental Institute, Princeton, NJ, USA, ¹⁸State Key Laboratory of Urban and Regional Ecology, Research Center for Eco-Environmental Sciences, Chinese Academy of Sciences, Beijing, China, ¹⁹Centre for Ocean and Atmospheric Sciences, School of Environmental Sciences, University of East Anglia, Norwich, UK, ²⁰NILU, Kjeller, Norway, ²¹Laboratoire des Sciences du Climat et de l'Environnement, LSCE-IPSL (CEA-CNRS-UVSQ), Université Paris-Saclay, Gif-sur-Yvette, France, ²²Climate and Ecosystem Sciences Division, Lawrence Berkeley National Lab, Berkeley, CA, USA

Abstract Nitrous oxide (N₂O) is a greenhouse gas and stratospheric ozone-depleting substance with large and growing anthropogenic emissions. Previous studies identified the influx of N₂O-depleted air from the stratosphere to partly cause the seasonality in tropospheric N₂O (aN₂O), but other contributions remain unclear. Here, we combine surface fluxes from eight land and four ocean models from phase 2 of the Nitrogen/N₂O Model Intercomparison Project with tropospheric transport modeling to simulate aN₂O at eight remote air sampling sites for modern and pre-industrial periods. Models show general agreement on the seasonal phasing of zonal-average N₂O fluxes for most sites, but seasonal peak-to-peak amplitudes differ several-fold across models. The modeled seasonal amplitude of surface aN₂O ranges from 0.25 to 0.80 ppb (interquartile ranges 21%–52% of median) for land, 0.14–0.25 ppb (17%–68%) for ocean, and 0.28–0.77 ppb (23%–52%) for combined flux contributions. The observed seasonal amplitude ranges from 0.34 to 1.08 ppb for these sites. The stratospheric contributions to aN₂O, inferred by the difference between the surface-troposphere model and observations, show 16%–126% larger amplitudes and minima delayed by ~1 month compared to Northern Hemisphere site observations. Land fluxes and their seasonal amplitude have increased since the pre-industrial era and are projected to grow further under anthropogenic activities. Our results demonstrate the increasing importance of land fluxes for aN₂O seasonality. Considering the large model spread, in situ aN₂O observations and atmospheric transport-chemistry models will provide opportunities for constraining terrestrial and oceanic biosphere models, critical for projecting carbon-nitrogen cycles under ongoing global warming.

Plain Language Summary Anthropogenic N₂O emissions, for example, from fertilizer use on agricultural land, fossil fuel burning, and some industrial activities, continue to increase atmospheric N₂O to values unprecedented for at least the past 800,000 years. This increase causes harmful global warming and stratospheric ozone depletion. Understanding how N₂O emissions from land and ocean influence atmospheric composition and climate is a research priority. Here, we address specifically how land and ocean emissions

Methodology: Qing Sun, Fortunat Joos, Sebastian Lienert

Project administration: Fortunat Joos, Hanqin Tian

Resources: Qing Sun, Fortunat Joos, Sarah Berthet, Dustin Carroll, Cheng Gong, Akihiko Ito, Atul K. Jain, Sian Kou-Giesbrecht, Angela Landolfi, Manfredi Manizza, Naiqing Pan, Pierre Regnier, Laure Resplandy, Roland Séférian, Hao Shi, Parvatha Suntharalingam, Rona L. Thompson, Hanqin Tian, Nicolas Vuichard, Sönke Zaehle, Qing Zhu

Software: Qing Sun, Fortunat Joos, Sebastian Lienert

Supervision: Fortunat Joos

Validation: Qing Sun

Visualization: Qing Sun

Writing – original draft: Qing Sun

Writing – review & editing: Qing Sun, Fortunat Joos, Sebastian Lienert, Sarah Berthet, Dustin Carroll, Cheng Gong, Akihiko Ito, Atul K. Jain, Sian Kou-Giesbrecht, Angela Landolfi, Manfredi Manizza, Naiqing Pan, Pierre Regnier, Laure Resplandy, Roland Séférian, Hao Shi, Parvatha Suntharalingam, Rona L. Thompson, Hanqin Tian, Nicolas Vuichard, Sönke Zaehle, Qing Zhu

contribute to the seasonality of N₂O at eight air monitoring sites. We apply surface N₂O fluxes simulated by eight land biosphere and four ocean biogeochemical models with a representation of lower atmosphere transport. This study complements earlier studies that show a strong influence on N₂O seasonality by the influx of N₂O-depleted air from the upper atmosphere. We demonstrate that land biosphere and ocean surface fluxes contribute substantially to the observed seasonal cycle at the different measurement sites. The surface contributions dampen the seasonal signal from the upper atmosphere and must be considered for explaining the observed N₂O seasonality. However, surface fluxes differ widely across models. In future work, atmospheric N₂O observations and transport modeling, considering both lower and upper atmospheric contributions, may help to better constrain biosphere models.

1. Introduction

Nitrous oxide (N₂O) is one of the main greenhouse gases (Canadell et al., 2021; Forster et al., 2021) and an ozone-depleting substance (Crutzen, 1970; Ravishankara et al., 2009). Its atmospheric mixing ratio (aN₂O) in the troposphere has increased from 271 ppb (parts per billion) since pre-industrial time to over 330 ppb in recent years (global average) (Lan, Thoning, & Dlugokencky, 2023; MacFarling Meure et al., 2006). The ice core records of aN₂O over the past 800,000 years (Schilt et al., 2010) and recent reconstructions of N₂O emissions using aN₂O and isotope data of ice cores show that anthropogenic contributions dominate this increase (Fischer et al., 2019; Park et al., 2012). The application of synthetic fertilizers since the green revolution is one of the main reasons for the increase in N₂O emissions (H. Tian et al., 2019). N₂O has an atmospheric lifetime of approximately 115 years (Canadell et al., 2021; Prather et al., 2015) before being removed in the stratosphere (Crutzen, 1970; Mueller, 2021). Therefore, the unprecedented rise in N₂O emissions and aN₂O poses multiple threats to natural systems and our society (IPCC, 2021, 2022).

As N₂O is predominantly produced by microbes in soils and waters (Bakker et al., 2014; Butterbach-Bahl et al., 2013), N₂O emissions are largely affected by environmental conditions which are under the influence of the changing climate and anthropogenic activities. Long-term changes in N₂O emissions and tropospheric aN₂O have been studied and reported for glacial-interglacial variations (Joos et al., 2020; Rubino et al., 2019; Schilt et al., 2010). For the modern period, the N₂O emissions from terrestrial ecosystems and the oceans have been investigated progressively across scales with site observations (e.g., Kock & Bange, 2015; Pastorello et al., 2020), field experiments (e.g., Breider et al., 2019; Dijkstra et al., 2012), as well as modeling (e.g., Martins et al., 2022; Landolfi et al., 2017; Xu-Ri & Prentice, 2008; Manizza et al., 2012). However, due to the complex processes of N₂O production in soils, inland waters and oceans (e.g., Battaglia & Joos, 2018; Ma et al., 2022; Hutchins & Capone, 2022) and loss in the stratosphere (Mueller, 2021), there is still poor understanding of the controls on tropospheric aN₂O and its seasonal and inter-annual variations.

Since the seasonality of aN₂O has been detected with high-precision measurements (Jiang et al., 2007), research on the seasonal and interannual net flux of stratosphere-troposphere exchange (STE) of N₂O has demonstrated its large impact on aN₂O seasonality (e.g., Nevison et al., 2011; Ruiz & Prather, 2022; Ruiz et al., 2021). aN₂O was also inverted using atmospheric transport models to derive surface N₂O fluxes (e.g., Bergamaschi et al., 2015; Hirsch et al., 2006; Thompson et al., 2019), which showed the importance of surface N₂O fluxes for aN₂O seasonality and interannual variability. As terrestrial ecosystems have been largely responding to climate and environmental changes, including the increasing atmospheric CO₂ concentration and enhanced N-fertilizer application (Tian et al., 2020; Walker et al., 2021), compared to pre-industrial times, the annual terrestrial emissions of N₂O have also increased in recent decades across the globe and with different intensities along the latitudinal zones (e.g., 2007–2016, see Figure 2 by Tian et al. (2020)). Due to the lack of global monthly anthropogenic N₂O emission estimates, some earlier studies could not consider the influence of the rising N₂O emissions from agriculture and natural terrestrial systems on aN₂O seasonality (Nevison et al., 2005). In contrast, more recent aN₂O inversion studies still typically used a limited set of N₂O surface flux estimates from ocean and land as priors (Liang et al., 2022; Patra et al., 2022; Thompson et al., 2014). Hence, information on how N₂O fluxes from land and ocean emissions, especially in the changing land biosphere, contribute to the seasonal variation in aN₂O is still lacking.

Table 1

Terrestrial Biosphere Models and Ocean Biogeochemical Models for N₂O Surface Fluxes in the NMIP-2 Ensemble and Descriptions

| Model | Reference | Resolution (degree) | Pre-industrial representation | Present-day representation |
|---------------------|--|---------------------|-------------------------------|----------------------------|
| Land fluxes | | | | |
| CLASSIC | Melton et al. (2020) | 0.5 | N/A | 2001–2020 |
| DLEM | Tian et al. (2015) | 0.5 | 1861–1880 | 2001–2020 |
| ELM | Zhu et al. (2019) | 0.5 | 1861–1880 | 2001–2020 |
| ISAM | Shu et al. (2020) | 0.5 | 1861–1880 | 2001–2020 |
| LPX-Bern | Lienert and Joos (2018) | 0.5 | 1861–1880 | 2001–2020 |
| OCN | Zaehle and Friend (2010) | 1 | 1861–1880 | 2001–2020 |
| ORCHIDEE | Vuichard et al. (2019) | 0.5 | 1861–1880 | 2001–2020 |
| VISIT | Ito et al. (2018) | 0.5 | 1861–1880 | 2001–2020 |
| Ocean fluxes | | | | |
| Bern3D | Battaglia and Joos (2018) | ca. 8 | 1861–1880 | 2001–2020 |
| UVic2.9 | Landolfi et al. (2017) | 1.8 × 3.6 | N/A | 2001–2019 |
| CNRM-ESM2-1 | Seferian et al. (2019) | 0.25 | N/A | 2001–2018 |
| ECCO-Darwin | Carroll et al. (2020), Ganesan et al. (2020) | 1/3 | N/A | 2001–2013 |

Note. N/A: not applicable.

Therefore, to assess the human impacts on aN₂O, there is a need to understand the response of aN₂O to the rapidly rising terrestrial N₂O emissions. In this study, we analyze the seasonal variations in N₂O flux estimates from eight Terrestrial Biosphere Models participating in the global Nitrogen/N₂O Model Inter-comparison Project (NMIP-2 (H. Tian et al., 2018, 2023)) and four ocean biogeochemical models. The flux patterns from these models are prescribed in an atmospheric transport matrix to simulate their contribution to the aN₂O seasonality at a set of air monitoring stations.

2. Materials and Methods

2.1. N₂O Emissions

N₂O fluxes from the land and ocean were simulated separately as part of the Nitrogen/N₂O Model Intercomparison Project (NMIP-2) (H. Tian et al., 2018). The soil emissions of N₂O from terrestrial ecosystems, both natural and agricultural lands, were modeled with eight process-based Terrestrial Biosphere Models (TBMs) and air-ocean fluxes with four Earth system/ocean biogeochemical models (Table 1). As the analysis for spatial data was carried out at 0.5° × 0.5° resolution, model outputs with different resolutions were regridded with a conservative remapping method. Natural fires and related biomass burning N₂O emissions are included in the TBM ensemble. Surface N₂O emissions from industry and fossil fuel (~1 TgN yr⁻¹), and from anthropogenic biomass burning, waste and wastewater, lightning, and inland and estuaries (~2 TgN yr⁻¹), totaling ca. 18% of overall emissions (~17 TgN yr⁻¹) for the period 2007–2016, are not included in our standard setup (for detailed estimates of source contributions see Tian et al., 2020). These sectorial emissions (industry, fossil) have a comparably small influence on aN₂O seasonality at the eight remote stations (amplitudes of 0.01–0.07 ppb), given their small magnitude (see Figure S1 in Supporting Information S1). All TBMs were forced with the same, NMIP-2, input data sets (Table 2). The climate data from 1901 to 1920 were recycled for the spin-up period and the 1850–1900 period of transient simulation. In addition, there is a control simulation for 171 years with recycled climate data from 1901 to 1920 and other forcing data fixed at the earliest available time (see Table 2). The control simulations show no drift in N₂O emissions, indicating an equilibrium state. Ocean emissions have a relatively small influence on modeled aN₂O seasonality (see Section 3), and we refer to H. Tian et al. (2020) and references in Table 1 for information on the 3-dimensional, dynamic ocean circulation-biogeochemistry models used to simulate ocean N₂O subsurface production from nitrification and denitrification and the resulting net exchange with the atmosphere. The ocean-model emissions are compared to observation-derived global climatology (Yang et al., 2020).

Table 2
Input Data Sets for NMIP-2 Terrestrial Biosphere Models

| Input data | Source/product | Period | Reference |
|---------------------------------|---|-----------|---|
| Climate | CRU-JRA55 | 1901–2020 | Harris (2021) |
| Atmospheric CO ₂ | Ice core CO ₂ data and NOAA annual observations | 1850–2020 | Joos and Spahni (2008); Lan, Tans, and Thoning (2023) |
| Land cover change | Land-Use Harmonization (LUH2) | 1850–2020 | Hurtt et al. (2020) |
| Atmospheric nitrogen deposition | International Global Atmospheric Chemistry (IGAC)/Stratospheric Processes and Their Role in Climate (SPARC) Chemistry-Climate Model Initiative (CCMI) | 1850–2020 | Hegglin et al. (2016) |
| Nitrogen fertilization | Harmonized Anthropogenic Nitrogen Input (HaNi) | 1911–2020 | Tian et al. (2022) |
| Manure nitrogen | Harmonized Anthropogenic Nitrogen Input (HaNi) | 1850–2020 | Tian et al. (2022) |

Two periods were considered in this study, namely pre-industrial (PI) from 1861 to 1880, and present day (PD) from 2001 to 2020 or depending on the available model outputs (pre-industrial N₂O fluxes from the ocean are only available for Bern3D, Table 1). The intra-annual variations of the land and ocean N₂O fluxes were calculated by detrending the flux time series, that is, monthly anomalies from 12-month running averages that are centered around zero by subtracting the overall mean.

2.2. Modeled Atmospheric N₂O Anomaly

The local aN₂O seasonal cycles were simulated at eight greenhouse gas monitoring stations, including two high-latitude stations (Alert and Barrow), one mid-latitude northern hemisphere station (Terceira Island), four tropical stations (Ragged Point, Christmas Island, Ascension Island, and Samoa), and one mid-latitude southern hemisphere station (Cape Grim). The selection of sites was limited by the availability of sites included in the transport matrix and for which long-term observational N₂O data are available (see Section 2.3). We use the Jacobian transport matrix determined by Kaminski et al. (1999) from a simulation with TM2, a global 3-dimensional model of the atmospheric transport of passive tracers (Heimann, 1995). The Jacobian matrix maps the influence of the surface flux from every grid cell and every month on aN₂O for a particular station and month. The matrix provides a convenient and cost-efficient way to quantify the basic impacts of surface fluxes on atmospheric tracer seasonality. Kaminski et al. (1999) applied TM2 with a horizontal resolution of ~10° × 8°, nine layers, a 4-hourly time step, and repeatedly cycling through the meteorological fields of the year 1987 from analyses of the European Center for Medium-Range Weather Forecast (ECMWF) adjusted for air mass conservation. Here, we use the transport matrix with surface N₂O fluxes from the previous 11 months and the current month when calculating the monthly aN₂O anomaly. The transport matrix covers the last 12 months with the implicit assumption that emissions older than 12 months have a small influence on the current aN₂O anomalies. This assumption appears justified given the small influence on aN₂O anomalies of emissions that were emitted 12 months before the evaluation of aN₂O at a given site (see Figures 3, 4, and 8 in Kaminski et al., 1999). Interannual variability in transport and its influence on aN₂O is not considered, while interannual aN₂O variability from surface flux variability is simulated and aN₂O seasonality varies across years. Stratospheric loss processes and the net flux of stratosphere-troposphere exchange (STE) on aN₂O seasonality are not represented by the TM2 matrix. Therefore, the simulated aN₂O seasonality from surface fluxes is expected to deviate from observations, given the importance of STE for aN₂O seasonality. We estimate the “stratospheric contribution” to aN₂O seasonality by the difference between the observation-derived seasonal anomalies and the modeled seasonal anomalies (from surface fluxes and tropospheric transport only). The stratospheric contribution arises from the seasonally varying dilution of tropospheric air by the exchange of stratospheric air with low N₂O. A weaker (larger) intrusion of stratospheric air than on average causes a positive (negative) anomaly in aN₂O.

In the standard setup, monthly N₂O fluxes from the land by the TBMs and the ocean surface by ocean biogeochemical models (Table 1) in both PI and PD periods are the input for computing aN₂O anomalies. In addition, land and ocean emissions were passed separately to the TM2 matrix to assess their individual influence on aN₂O seasonality. Furthermore, the impacts on monthly aN₂O anomalies by the detrended intra-annual variations in flux versus those from the deseasonalized spatial flux pattern were separately quantified. Accordingly, the detrended N₂O fluxes from the land and ocean, that is, monthly anomalies from 12-month running averages that are centered around zero by subtracting the overall mean, were used to simulate the aN₂O anomaly caused by the intra-annual variation of N₂O emissions. The 12-month running averages of the fluxes, as deseasonalized fluxes, were used to estimate the influence of the mean spatial pattern and long-term trend of N₂O emissions on aN₂O at each station. The sum of aN₂O anomaly simulated with these

Table 3
Selected NOAA/CCGG Stations and Their Seasonal Amplitude of Atmospheric N₂O Mixing Ratio (ppb; Mean ±1 Standard Deviation From Interannual Variability) Observed by Flask Measurements Since 2000

| Code | Name | Location | | Altitude (m a.s.l.) | Number of monthly data | Min-to-max amplitude |
|------|------------------|----------|---------|---------------------|------------------------|----------------------|
| ALT | Alert | 82.5°N | 62.5°W | 210 | 17–18 | 0.95 ± 0.30 |
| BRW | Barrow | 71.3°N | 156.6°W | 475 | 18–19 | 1.08 ± 0.23 |
| AZR | Terceira Island | 38.8°N | 27.3°W | 19 | 3–5 | 0.34 ± 0.18 |
| RPB | Ragged Point | 13.2°N | 59.4°W | 45 | 17–18 | 0.52 ± 0.17 |
| CHR | Christmas Island | 1.7°N | 157.2°W | 0 | 6–9 | 0.73 ± 0.54 |
| ASC | Ascension Island | 7.9°S | 14.4°W | 54 | 15–16 | 0.55 ± 0.18 |
| SMO | Samoa | 14.3°S | 170.6°W | 42 | 17–18 | 0.98 ± 0.25 |
| CGO | Cape Grim | 40.7°S | 144.7°E | 164 | 16–17 | 0.81 ± 0.30 |

Note. Note that at AZR and CHR, the seasonality analysis is limited by the data availability with fewer 12-month continuous measurements, therefore less robust than at other sites.

decomposed fluxes, that is, detrended and deseasonalized, matches aN₂O anomaly simulated in the standard setup. For the total contribution from land and ocean surface flux to aN₂O seasonality, each individual land output was combined with every ocean output, resulting in 32 members of the total surface flux.

2.3. Atmospheric N₂O Seasonality Observations

The atmospheric N₂O mixing ratios (aN₂O) for the selected stations were obtained from surface flask measurements by the National Oceanic and Atmospheric Administration (NOAA) Carbon Cycle Greenhouse Gases (CCGG) of the CCGG SurfaceFlask v2.0 ObsPack available at weekly to biweekly frequency (Dlugokencky et al., 2021) (Table 3). Data for the selected stations (Alert, Barrow, Terceira Island, Ragged Point, Samoa, Christmas Island, Ascension Island, and Cape Grim) were available from 2000 to 2019. Months with missing values were omitted; therefore, the number of data available for each month differed (Table 3). The observation-based seasonal aN₂O anomaly was calculated from the detrended time series, that is, the difference from 12-month running averages that are centered around zero by subtracting the overall mean. The observation-based, period-mean seasonality of aN₂O is computed from the aN₂O anomalies weighted by the measurement uncertainties which are included in the data sets. We averaged data for individual months separately to avoid potential biases, without gap-filling, for seasonality estimates to the extent possible. The measurement uncertainty is typically 0.26 ppb for biweekly values; the nominal uncertainty of the average of, for example, 36 biweekly data would then be 0.04 ppb. The amplitude of aN₂O seasonality is determined as the min-to-max difference for each year.

2.4. Data Analysis

Data analysis and plotting were carried out in Python (Van Rossum & Drake, 1995) with packages xarray (Hoyer & Hamman, 2017), pandas (The pandas development team, 2020), and matplotlib (Hunter, 2007). The seasonality of modeled N₂O fluxes and aN₂O is the temporal mean intra-annual variation over the investigated periods for each individual model and for the multi-model median. The seasonal amplitude of modeled N₂O fluxes and aN₂O is determined as the min-to-max difference of monthly fluxes or monthly mean mixing ratio on a yearly basis for each model. The multi-model median and quartiles of the seasonal amplitude are calculated from the long-term mean seasonal amplitudes of all the models as well as all the combinations of land and ocean models.

3. Results

3.1. Seasonality in Modeled N₂O Emissions

3.1.1. Land Emissions

The multi-model medians of N₂O emissions show large intra-annual and spatial heterogeneity on land (red lines) and ocean (blue lines, Figures 1d–1f). In austral summer (December, January, and February; DJF), high land

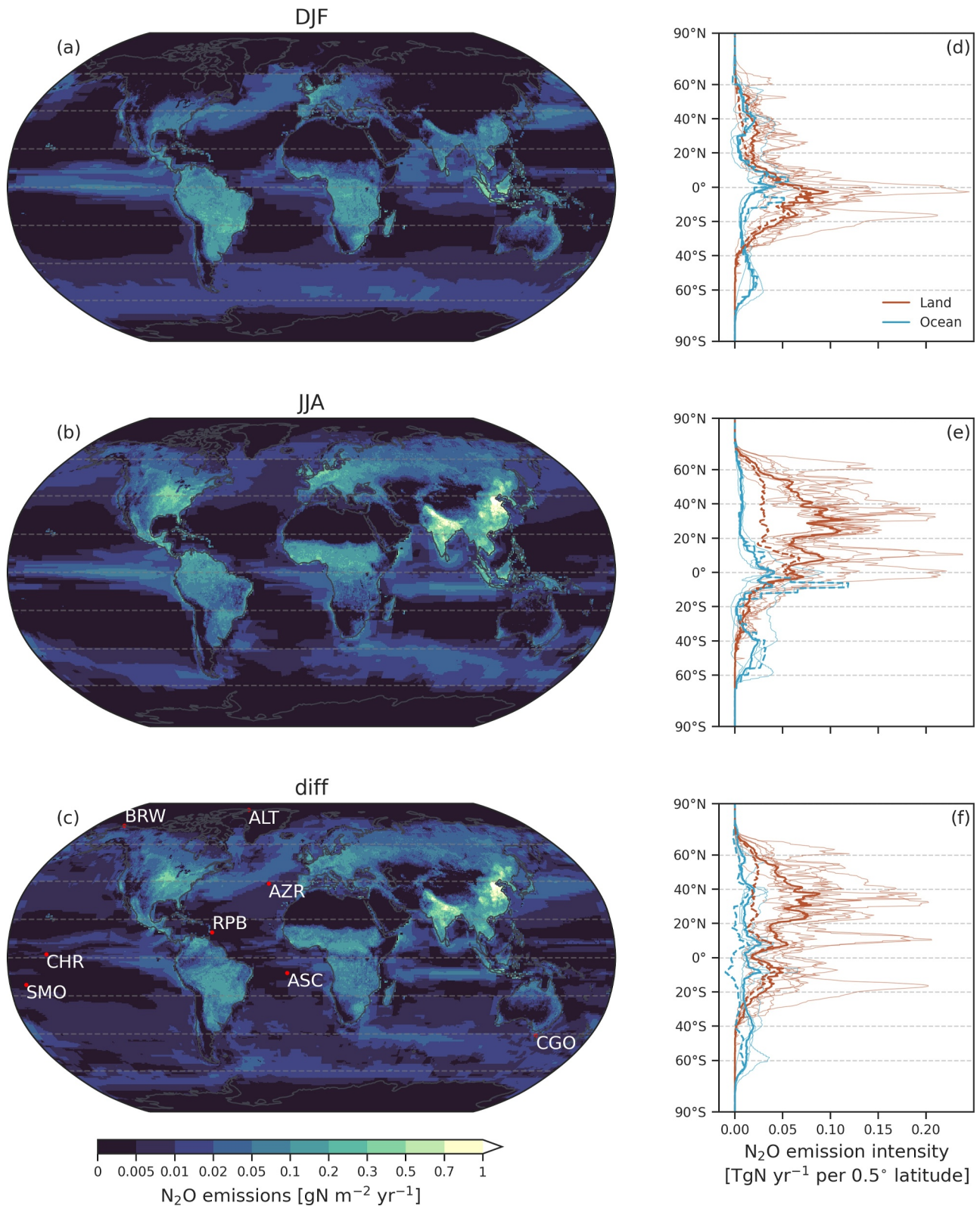


Figure 1.

emissions are simulated for the Southern Hemisphere (SH) in the tropics (0° – 20° S, 2.7 TgN yr^{-1} , multi-model median) and subtropics (20° S– 40° S, 0.85 TgN yr^{-1} , Figures 1a and 1d; Table 4) for the present-day period (PD; 2001–2020). Global average emissions for DJF (PI: 6.17 TgN yr^{-1}) grew 36% since the pre-industrial period (PI, 1861–1880: 4.55 TgN yr^{-1}), with increases in all latitudinal zones (0.01 – 0.43 TgN yr^{-1} , Figure 1d; Table 4). In boreal summer (June, July, and August; JJA), high emissions are simulated for the Northern Hemisphere (NH) in the subtropics (20° N– 40° N, 3.62 TgN yr^{-1}), tropics (0° – 20° N, 2.78 TgN yr^{-1}), and temperate zone (40° N– 60° N, 2.20 TgN yr^{-1} , Figures 1b and 1e; Table 4). In these regions, average emissions for JJA also noticeably increased from the PI to PD by 2.41 (200%), 0.92 (49%), and 1.09 (98%) TgN yr^{-1} , respectively (Figure 1e; Table 4). The global average emissions for JJA grew by 81% and 4.76 TgN yr^{-1} . The seasonal difference (IDJF–JJA) in terrestrial N_2O emissions is substantial between 20° S and 60° N with maxima in 20° N– 40° N (Figures 1c and 1f; Table 4), though the seasonal difference is, on average, close to zero near the equator. Seasonality in emissions also increased from the PI to PD (Figure 1f; Table 4). In addition, the N_2O emissions simulated by the eight TBMs range widely in both seasons and seasonal differences for PD as well as PI period (Figure 1; Table 4) where the large interquartile ranges coincide with high emission regions (Figure S2 in Supporting Information S1).

The seasonality of land N_2O fluxes was separated by latitudinal regions (Figure 2). The regions with high seasonal differences in N_2O emissions (Table 4) as well as the regions with the highest annual N_2O emissions (Table 5) in the NH (20° N– 40° N, 0° – 20° N, and 40° N– 60° N) show emissions peaking in June–August and a long-term mean seasonal amplitude of 3.84, 1.82, and 2.42 TgN yr^{-1} (multi-model median), respectively (Figures 2b–2d; Table 5). The seasonal amplitudes of N_2O emissions from individual land models differ by 2–5 folds in these regions. In the SH, the land emissions show the opposite phasing compared to the NH. The N_2O emissions from 0° – 20° S have the strongest seasonality, with a peak in January and an ensemble-median amplitude of 2.04 TgN yr^{-1} . The model spread is large and seasonal amplitudes differ by more than seven folds among the land models (Figure 2e). Land N_2O emissions between 60° N– 90° N and 20° S– 40° S are comparably low and show very weak intra-annual variations in absolute terms (Figures 2a and 2f; Table 5).

Compared to the PI period, the global terrestrial N_2O emissions increased by 36% while the seasonal amplitude increased by 81% (Table 5). The seasonal amplitude of terrestrial N_2O emissions in the SH increased by 18% for 0° – 20° S and by 107% for 20° S– 40° S. The increase in amplitude is even larger for the NH land, with 35%–108% for 0° – 20° N, 20° N– 40° N, and 40° N– 60° N (Figure 2; Table 5).

3.1.2. Ocean Emissions

Monthly ocean N_2O emissions are lower with less intra-annual variation compared to land emissions (Figures 1 and 3; Tables 4 and 5). Seasonal mean ocean emissions during PD show similar patterns during DJF and JJA, with relatively higher emissions from 0° – 20° N, 0° – 20° S, and 40° – 60° S in both seasons (median of 0.53 – 0.84 TgN yr^{-1}). The absolute differences between DJF and JJA are the highest for 0° – 20° S (0.32 TgN yr^{-1}) and 60° – 90° S (0.16 TgN yr^{-1}), while they amount to less than 0.37 TgN yr^{-1} in other regions and globally only 0.02 TgN yr^{-1} (Table 4). Pre-industrial (PI) N_2O fluxes from the ocean are only available from Bern3D; therefore, they cannot be compared directly with the multi-model median. The modeled changes in ocean emissions since the PI periods are comparably low in all regions (Figure 1f).

Similar to land emissions, the ocean N_2O emissions also show distinct seasonal cycles with different phasing between the NH and SH for PD (Figure 3). The long-term seasonal amplitudes for most latitudinal zones differ by 3–8 folds among the ocean models. However, the seasonal amplitudes of ocean N_2O emissions are usually much smaller than that of land N_2O emissions (ocean: median of up to 1.12 TgN yr^{-1} ; land: median of up to 3.84 TgN yr^{-1} for different regions, Table 5), and the seasonality of ocean N_2O emissions remains approximately constant from the PI to PD for Bern3D (Figure 3). A reconstructed global climatology for monthly ocean N_2O emissions

Figure 1. Long-term average N_2O emission density (multi-model median) in recent decades (present day, PD; 2001–2020), from the land and ocean ($\text{gN m}^{-2} \text{ yr}^{-1}$) for DJF (a, December, January, and February), JJA (b, June, July, and August), and the absolute differences between these two seasons (c), as well as the emissions (TgN yr^{-1} ; dark lines: multi-model median; light lines: ensemble members) along the latitudinal gradient resolved by 0.5° for both the land (red lines) and the ocean (blue lines) during PD (solid lines) and pre-industrial period (PI; 1861–1880, dashed lines) (d–f). The selected NOAA/CCG stations are marked by red points in (c) (ALT: Alert, BRW: Barrow, AZR: Terceira Island, RPB: Ragged Point, CHR: Christmas Island, ASC: Ascension Island, SMO: Samoa, CGO: Cape Grim). Pre-industrial N_2O fluxes from the ocean are only available for Bern3D.

Table 4

Multi-Model Seasonal N₂O Net Surface-To-Atmosphere Fluxes From the Land and the Ocean for Present Day (2001–2020) and Pre-Industrial (1861–1880) Periods From Different Latitudinal Zones (TgN yr⁻¹) in DJF (December, January, and February), JJA (June, July, and August), and the Absolute Differences Between These Two Seasons

| Latitude | Land | | | Ocean | | |
|----------------------------|--------------------|---------------------|--------------------|--------------------|-------------------|-------------------|
| | DJF | JJA | DJF-JJA | DJF | JJA | DJF-JJA |
| Present day (2001–2020) | | | | | | |
| 60°N–90°N | 0.02 [0.00, 0.05] | 0.35 [0.14, 0.72] | 0.32 [0.60, 0.12] | 0.01 [-0.03, 0.05] | 0.08 [0.05, 0.12] | 0.07 [0.15, 0.00] |
| 40°N–60°N | 0.42 [0.22, 0.75] | 2.20 [1.24, 3.63] | 1.62 [2.99, 0.76] | 0.37 [0.18, 0.65] | 0.27 [0.21, 0.36] | 0.11 [0.12, 0.39] |
| 20°N–40°N | 0.79 [0.46, 1.46] | 3.62 [2.43, 5.47] | 2.48 [4.20, 1.35] | 0.37 [0.10, 0.83] | 0.25 [0.19, 0.38] | 0.12 [0.16, 0.53] |
| 0°–20°N | 1.36 [0.79, 2.51] | 2.78 [1.77, 4.56] | 1.18 [2.55, 0.29] | 0.81 [0.47, 1.43] | 0.79 [0.51, 1.28] | 0.01 [0.42, 0.49] |
| 0°–20°S | 2.70 [1.60, 4.47] | 1.29 [0.77, 2.52] | 1.02 [0.16, 2.38] | 0.53 [0.37, 0.97] | 0.84 [0.48, 1.76] | 0.32 [0.87, 0.05] |
| 20°S–40°S | 0.85 [0.52, 1.46] | 0.36 [0.20, 0.62] | 0.43 [0.16, 0.91] | 0.33 [0.27, 0.47] | 0.32 [0.05, 0.81] | 0.01 [0.42, 0.30] |
| 40°S–60°S | 0.03 [0.02, 0.05] | 0.03 [0.02, 0.04] | 0.00 [0.01, 0.01] | 0.68 [0.52, 0.83] | 0.67 [0.36, 1.04] | 0.02 [0.39, 0.32] |
| 60°S–90°S | NaN | NaN | NaN | 0.22 [0.15, 0.32] | 0.03 [0.01, 0.09] | 0.16 [0.07, 0.27] |
| Global | 6.17 [3.62, 10.75] | 10.63 [6.56, 17.58] | 4.15 [10.03, 0.78] | 3.33 [2.02, 5.55] | 3.26 [1.85, 5.83] | 0.02 [2.46, 2.24] |
| Pre-industrial (1861–1880) | | | | | | |
| 60°N–90°N | 0.01 [0.00, 0.05] | 0.28 [0.12, 0.70] | 0.26 [0.57, 0.11] | –0.03 | 0.07 | 0.10 |
| 40°N–60°N | 0.15 [0.06, 0.34] | 1.11 [0.59, 1.94] | 0.85 [1.59, 0.40] | 0.43 | 0.26 | 0.17 |
| 20°N–40°N | 0.37 [0.18, 0.65] | 1.21 [0.74, 2.17] | 0.74 [1.62, 0.34] | 0.31 | 0.23 | 0.08 |
| 0°–20°N | 1.08 [0.57, 2.23] | 1.86 [1.08, 3.35] | 0.56 [1.60, 0.10] | 1.07 | 0.92 | 0.15 |
| 0°–20°S | 2.29 [1.22, 3.95] | 1.16 [0.59, 2.35] | 0.72 [0.03, 2.00] | 1.02 | 1.93 | 0.90 |
| 20°S–40°S | 0.63 [0.34, 1.13] | 0.23 [0.11, 0.46] | 0.26 [0.10, 0.69] | 0.29 | 0.43 | 0.14 |
| 40°S–60°S | 0.02 [0.01, 0.03] | 0.01 [0.00, 0.02] | 0.00 [0.00, 0.01] | 0.71 | 1.07 | 0.36 |
| 60°S–90°S | NaN | NaN | NaN | 0.19 | 0.07 | 0.13 |
| Global | 4.55 [2.38, 8.38] | 5.86 [3.24, 11.00] | 1.41 [5.31, 1.95] | 4.00 | 4.96 | 0.97 |

Note. Multi-model median and [25th percentile, 75th percentile] of long-term model average are given. Pre-industrial N₂O fluxes from the ocean are only available for Bern3D. N/A: not applicable.

from surface N₂O measurements by Yang et al. (2020) shows comparable seasonality for all latitudinal zones (blue circles in Figure 3).

3.2. Seasonality in Observed and Modeled Atmospheric N₂O

The local aN₂O modeled from land and ocean N₂O fluxes show seasonal cycles, which vary in phase and amplitude for different stations (solid black lines in Figure 4; Table 6). We recall that the net flux from the troposphere-stratosphere exchange is not included in the model, and thus the mismatch between observation and model results largely represents the stratospheric contribution, that is, the seasonally varying dilution of tropospheric air by the exchange of stratospheric air with low N₂O (yellow lines in Figure 4; Tables 3 and 6). At the northern high-latitude stations Alert (ALT) and Barrow (BRW), the modeled aN₂O have seasonal cycles with amplitudes of 0.70 and 0.77 ppb (multi-model median) and October maxima during the PD, while the observed seasonal amplitudes are 0.95 ± 0.3 and 1.08 ± 0.22 ppb (long-term mean ± 1 standard deviation), respectively and have maxima in February-March (gray dots in Figure 4; Table 3). At the northern mid-latitude station Terceira Island (AZR) and the tropical station Ragged Point (RPB), the modeled aN₂O seasonal cycle shows similar patterns to the northern high-latitude stations, with October maximum and an amplitude of 0.60 and 0.58 ppb, respectively, larger than (0.34 ± 0.18 ppb) or close to (0.52 ± 0.17 ppb) observed seasonal amplitude. However, the observed seasonal cycle at these four NH stations is out-of-phase with the modeled cycle with a ca. 5-month delay in maxima. The estimated stratospheric contribution is out-of-phase with respect to the modeled contribution from fluxes and has a larger amplitude at these four NH stations (multi-model median of 1.47, 1.74, 0.70,

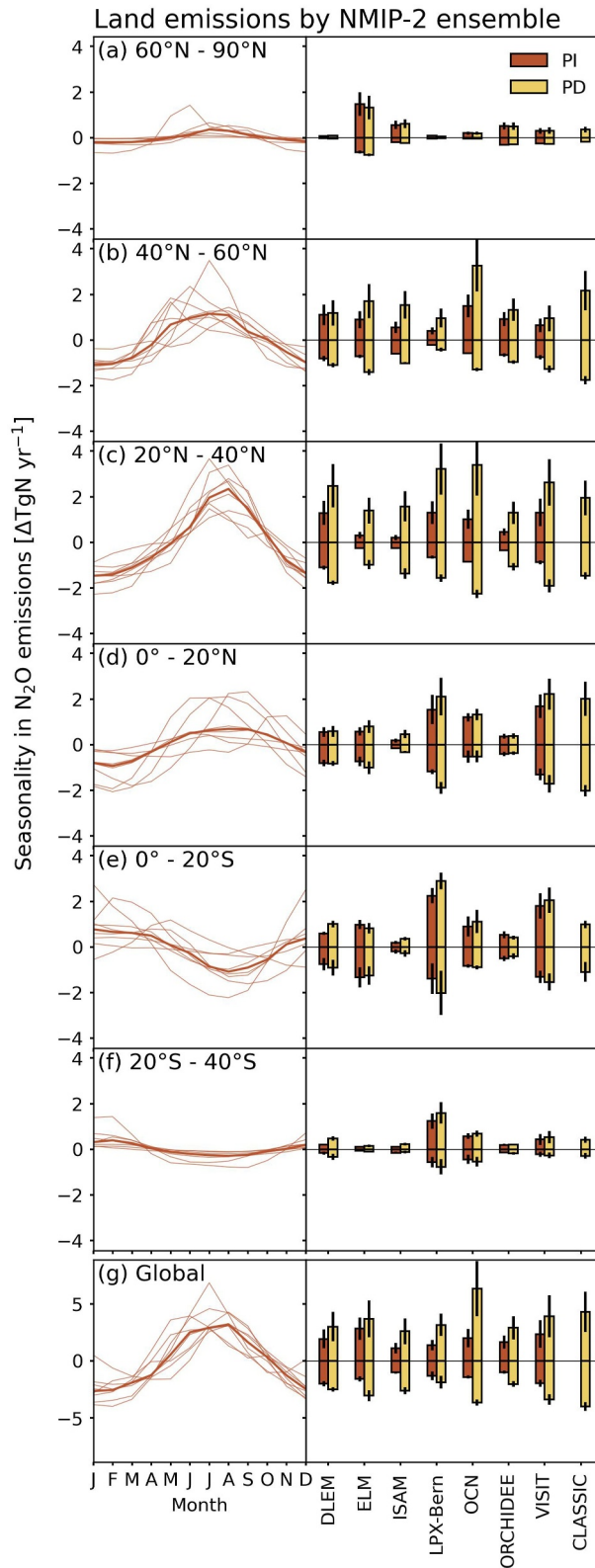


Figure 2.

and 0.81 for ALT, BRW, AZR, and RPB; Table 6). At other tropical and the SH stations, Christmas Island (CHR), Ascension Island (ASC), and Samoa (SMO) in the tropics and Cape Grim (CGO) in the mid-latitudes, the modeled aN_2O shows less clear seasonal patterns compared to the NH stations. The modeled seasonal amplitude at CHR and ASC are both 0.47 ppb with a March and February maximum and the observed amplitude is 0.73 ± 0.53 ppb and 0.55 ± 0.18 ppb with matching maxima; the modeled amplitude at SMO is 0.39 ppb, much lower than observed (0.98 ± 0.25 ppb), and the maximum occurs in February in the model and January in the observations; with individual models largely differing in phasing, the modeled amplitude for CGO is the lowest of the eight stations at 0.28 ppb, with a February maximum, and also much lower than observed (0.81 ± 0.30), with a December maximum (Figure 4; Tables 3 and 6). The stratospheric contributions at these stations are estimated to have similar seasonal amplitudes to the observed (multi-model median of 0.58, 0.63, 0.82, and 0.89 for CHR, ASC, SMO, and CGO). The interquartile ranges of the seasonal aN_2O amplitude from uncertainties in surface model fluxes are between 26% and 52% of the median for the eight stations, while the interquartile ranges of the estimated stratospheric contribution are between 11% and 15% (except at AZR, 20% and RBP, 42%; Figure 5; Table 6).

3.2.1. Contributions From Land Versus Ocean N_2O Emissions

When transporting N_2O emissions from the land (solid red lines in Figure 5) and the ocean (solid blue lines in Figure 5) separately, the corresponding aN_2O seasonal cycles differ by phasing and amplitude at all stations (Figure 5; Table 6). The seasonal aN_2O amplitude resulting from land N_2O emissions (0.25–0.80 ppb, multi-model median) is generally larger than from ocean N_2O emissions (0.14–0.21 ppb) except for CGO (0.25 ppb from both land and ocean; Table 6). Moreover, due to the differences in seasonal aN_2O phasing from land versus ocean fluxes, the modeled aN_2O seasonal amplitudes from only land emissions are slightly larger than those from total emissions at NH stations (by 0.01–0.08 ppb), and smaller at SH stations (by 0.02–0.07 ppb; Table 6). Furthermore, the modeled aN_2O seasonality from total N_2O emissions has a similar phasing compared to that from only land emissions at all stations, except for CGO, where ocean emissions strongly influence aN_2O seasonality (Figure 5; Table 6). The interquartile ranges of the seasonal aN_2O amplitude are between 21% and 52% of the median from uncertainties in land model fluxes and between 17% and 68% from uncertainties in ocean model fluxes for the eight stations.

For the pre-industrial (PI) period, modeled aN_2O seasonal cycles have a similar phasing to that of PD (dashed lines for PI and solid lines for PD in Figure 5). The PI ocean N_2O emissions are only available by Bern3D, showing small PD-PI differences (Figure 5). The seasonal amplitudes attributed to land N_2O fluxes increase at least by 26% at all stations (PI: 0.19–0.49 ppb; PD: 0.25–0.80 ppb, Table 6), with the largest PD-PI differences at the northern high-latitude stations (ALT and BRW) by 0.29 and 0.31 ppb (61% and 64%, Table 6).

3.2.2. Influence of Intra-Annual Variation Versus Spatial Pattern of N_2O Emissions

Next, we quantify the contributions to aN_2O seasonality resulting from the intra-annual variations in flux versus those from the deseasonalized spatial flux pattern. The deseasonalized spatial pattern can cause seasonal variations in aN_2O due to seasonally varying atmospheric transport. The intra-annual variation is obtained by using the detrended N_2O fluxes as sources for the atmospheric transport model, while the remaining influence is obtained by the running mean of N_2O fluxes (ALT, SMO in Figure 6; BRW, AZR, RPB, CHR, ASC, CGO in Figure S3 in Supporting Information S1). Besides, industrial emissions that do not vary by season could also contribute to the spatial pattern but are not considered in this study.

At the NH stations (ALT, BRW, AZR, and RPB), the (detrended) seasonal cycle of N_2O emissions leads to similar phasing and amplitude for aN_2O seasonality (multi-model median: 0.66, 0.71, 0.58, and 0.46 ppb, respectively) as when using total absolute emissions (Figure 6 and Figure S3, Table S1 in Supporting Information S1). The seasonal amplitude of aN_2O from 12-month running mean fluxes is small (0.17–0.21 ppb, Table S1 in Supporting Information S1), suggesting both land and ocean N_2O emissions contribute to the

Figure 2. Long-term average seasonality of N_2O emissions for present day (PD, 2001–2020) for different latitudinal zones, and the seasonal minimum and maximum of emissions anomalies for each zone (right panels) during pre-industrial (PI, 1861–1880) and PD periods simulated by NMIP-2 land models, respectively. The vertical lines in the right panels indicate ± 1 standard deviation from temporal variability around the period means. Thick lines indicate multi-model median and thin lines indicate individual models in the left panels.

Table 5
Modeled Net Land and Ocean Annual N₂O Fluxes to the Atmosphere From Different Latitudinal Zones (TgN yr⁻¹) and Seasonal Amplitude (TgN yr⁻¹), Quantified by the Difference Between Minimum and Maximum Flux, for Present Day (2001–2020) and Pre-Industrial (1861–1880) Periods

| Latitude | Land | | Ocean | |
|----------------------------|---------------------|----------------------|-------------------|----------------------|
| | Annual flux | Min-to-max amplitude | Annual flux | Min-to-max amplitude |
| Present day (2001–2020) | | | | |
| 60°N–90°N | 0.21 [0.05, 0.37] | 0.56 [0.22, 0.82] | 0.03 [0.01, 0.05] | 0.16 [0.12, 0.19] |
| 40°N–60°N | 1.60 [1.38, 1.92] | 2.42 [2.27, 3.32] | 0.30 [0.24, 0.44] | 0.67 [0.37, 0.73] |
| 20°N–40°N | 2.61 [2.45, 2.76] | 3.84 [2.80, 4.60] | 0.25 [0.18, 0.31] | 0.49 [0.30, 0.76] |
| 0°–20°N | 2.77 [2.18, 3.01] | 1.82 [1.26, 3.96] | 0.94 [0.54, 1.14] | 0.77 [0.33, 0.81] |
| 0°–20°S | 2.37 [2.01, 3.04] | 2.04 [1.64, 2.46] | 1.26 [0.48, 1.43] | 1.12 [0.28, 1.13] |
| 20°S–40°S | 0.78 [0.62, 0.90] | 0.75 [0.38, 0.92] | 0.20 [0.19, 0.24] | 0.56 [0.42, 0.58] |
| 40°S–60°S | 0.03 [0.02, 0.04] | 0.02 [0.02, 0.03] | 0.57 [0.47, 0.66] | 0.73 [0.48, 1.04] |
| 60°S–90°S | N/A | N/A | 0.09 [0.07, 0.22] | 0.24 [0.18, 0.34] |
| Global | 10.51 [9.80, 11.21] | 6.13 [5.17, 7.56] | 3.76 [2.91, 4.19] | 2.26 [2.11, 2.40] |
| Pre-industrial (1861–1880) | | | | |
| 60°N–90°N | 0.19 [0.05, 0.42] | 0.55 [0.19, 0.79] | 0.01 | 0.13 |
| 40°N–60°N | 0.92 [0.67, 1.02] | 1.58 [1.27, 1.77] | 0.28 | 0.75 |
| 20°N–40°N | 1.02 [0.87, 1.21] | 1.85 [0.69, 2.07] | 0.20 | 0.54 |
| 0°–20°N | 2.03 [1.89, 2.37] | 1.35 [1.05, 2.23] | 0.97 | 0.82 |
| 0°–20°S | 2.23 [2.00, 2.50] | 1.73 [1.20, 2.72] | 1.47 | 1.21 |
| 20°S–40°S | 0.60 [0.48, 0.64] | 0.36 [0.30, 0.84] | 0.27 | 0.60 |
| 40°S–60°S | 0.02 [0.01, 0.02] | 0.01 [0.01, 0.02] | 0.71 | 1.16 |
| 60°S–90°S | N/A | N/A | 0.08 | 0.26 |
| Global | 7.73 [6.21, 8.03] | 3.39 [2.66, 4.11] | 3.99 | 2.37 |

Note. Multi-model median and [25th percentile, 75th percentile] of long-term model average are given. Pre-industrial N₂O fluxes from the ocean are only available for Bern3D. N/A: not applicable.

seasonality of aN₂O mainly via their seasonal cycles at the NH stations. At the tropical stations (CHR, ASC, and SMO), both phasing and amplitude of aN₂O seasonality are affected slightly more by the spatial pattern (amplitude of 0.41, 0.35, and 0.28 ppb) than the seasonality of N₂O fluxes (0.31, 0.28, and 0.23 ppb, Figure 6 and Figure S3, Table S1 in Supporting Information S1). For the SH mid-latitude station CGO, land N₂O fluxes have similar impacts on the aN₂O seasonal amplitude via their spatial pattern (0.19 ppb) than their seasonality (0.21 ppb), while ocean fluxes have a stronger impact via their seasonality (0.22 ppb) than their spatial pattern (0.06 ppb). The combined fluxes show a larger impact via their seasonality (0.28 ppb) than their spatial pattern (0.14 ppb). In summary, the impacts of temporal variation and spatial patterns of N₂O fluxes at these remote sites differ largely by latitude.

4. Discussion

Our results show large spatial and temporal variations and a pronounced seasonality in N₂O surface-to-atmosphere fluxes. The variations and seasonality of N₂O emissions from the land biosphere are stronger than those from the ocean. The largest increase in the seasonal amplitude of emissions over the industrial period (1861–1880 to 2001–2020) was found over land between 20°N and 40°N, with an industrial period increase in the seasonal amplitude of 108% (multi-model median; Table 5). The increasing land emissions are attributed, using the factorial simulations of the NMIP project (Tian et al., 2018), to anthropogenic causes. The responsible activities mainly include fertilizer applications in arable lands (see Cardenas et al., 2013; Fuchs et al., 2020; Tian et al., 2019) and land-use change such as converting natural land cover to intensively managed croplands or

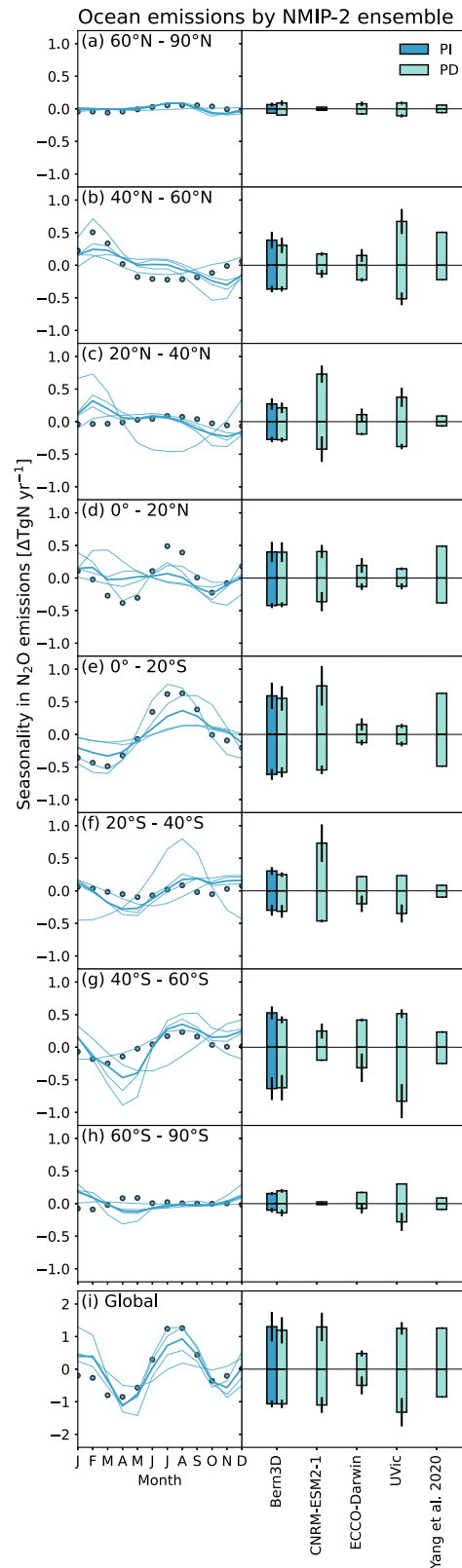


Figure 3.

pasture (Petitjean et al., 2015). Notably, these also tend to exaggerate the existing intra-annual variations in soil microbial activities by alternating soil N availability (e.g., Feigenwinter et al., 2023). However, the increased soil N₂O emissions in croplands due to fertilization can occur prior to or after the growing season and are subject to plant N demand as well as environmental conditions (Maier et al., 2022; Merbold et al., 2014). This leaves the link between the timing of fertilizer applications and the seasonal cycle of N₂O emissions from croplands unclear. Besides, considerable model spread in seasonal emissions (Figure 1 and Figure S2 in Supporting Information S1) and min-to-max amplitude (Figures 2 and 3) of N₂O emissions are noted for all latitudinal zones.

Modern land and ocean N₂O fluxes contribute to tropospheric N₂O (aN₂O) seasonality to different extents at different stations (Figure 5; Table 6). The seasonality of aN₂O is the combined result of seasonally and spatially varying atmospheric transport and seasonally and spatially varying fluxes. For all stations except CGO, land N₂O emissions influence aN₂O seasonality more than ocean N₂O emissions, predominantly via their seasonal cycles at NH stations (ALT, Figure 6; BRW, AZR, and RBP, Figure S3 and Table S1 in Supporting Information S1) while mainly via deseasonalized spatial patterns at remote tropical stations in the SH (SMO, Figure 6; CHR and ASC, Figure S3 and Table S1 in Supporting Information S1). At CGO, ocean N₂O fluxes show a slightly stronger impact on aN₂O seasonality via their seasonal cycles (Figure S3 and Table S1 in Supporting Information S1). These results suggest that total fluxes as opposed to detrended fluxes should be used to quantify the overall influence of N₂O emissions on aN₂O seasonality.

Generally, the measured aN₂O seasonality is considered to be an outcome of seasonal surface emissions, tropospheric transport, stratospheric loss, and stratosphere-to-troposphere exchange (STE) (e.g., Bouwman & Taylor, 1996; Nevison et al., 2005; Ruiz et al., 2021). Our simulated aN₂O seasonality using TM2 represents only the contribution from surface fluxes and predominantly tropospheric transport, whereas stratospheric N₂O loss and resulting net fluxes by STE are not included. Thus, the mismatch between our modeled and the observed aN₂O seasonality (Figure 4, yellow lines) can be understood to represent the stratospheric contribution to the aN₂O seasonal cycle, with some uncertainty due to the uncertainties in modeling surface N₂O emissions and atmospheric transport (see also Figure 5 of Ruiz et al. (2021) and Figure 5 of Ruiz and Prather (2022)). The stratospheric contribution stems from the seasonally varying dilution of tropospheric air by the exchange of stratospheric air with low N₂O. At the northern hemisphere (NH) sites (ALT, BRW, AZR, and RPB), the estimated stratospheric contributions to aN₂O (Figure 4) result in a minimum in August–September, nearly 6 months out-of-phase with the contributions from surface fluxes. As the stratosphere is the main sink for N₂O, stratospheric air is therefore depleted in N₂O, and the minimum in the seasonal cycle caused by the stratosphere-troposphere exchange indicates the highest stratospheric contribution (Yu et al., 2020). The stratospheric contributions have large amplitudes and apparently dominate the observed seasonality at these NH sites, particularly at the high-altitude sites ALT and BRW. The phasing of our estimated stratospheric contributions is consistent with a stratospheric tracer of N₂O modeled using the chemistry-transport model LMDz6 (following the method outlined in (Ruiz & Prather, 2022), purple lines in Figure 4) with a maximum influence of STE in August and September in the northern extratropics. Research using stable N isotopes to infer the mixing of N₂O from the stratosphere and surface emissions also agrees with the highest contributions from stratospheric exchange at a NH site, Jungfraujoch, in August (observation over 2014–2018) (Yu et al., 2020) as well as average in the NH in August–September (simulation over 2000–2019) (Liang et al., 2022). At the tropical sites (CHR, ASC, and SMO), there is less influence from STE, and thus the observed seasonality of aN₂O is likely mostly driven by land emissions and tropospheric transport. At the southern hemisphere (SH) mid-latitude site CGO, our estimated stratospheric contribution has a minimum in March–June (Figure 4) and is thus nearly 6 months out-of-phase with the NH, as expected. The stratospheric influence at CGO reported by Nevison et al. (2005), from the source contributions to aN₂O seasonality, and inferred by Park et al. (2012), from δ¹⁵N seasonality, both show similar phasing (April and June minima, respectively) to our estimated stratospheric influence. Furthermore, the amplitude of the estimated stratospheric contribution is much smaller than in the NH (Table 6), which again is as expected owing to the smaller seasonal amplitude of the STE net fluxes in the SH (James et al., 2003; Liang

Figure 3. Long-term average seasonality of N₂O emissions for present day (PD, 2001–2020) for different latitudinal zones, and the seasonal minimum and maximum of emissions anomalies for each zone (right panels) during pre-industrial (PI, 1861–1880) and PD periods simulated by NMIP-2 ocean models, respectively. The vertical lines in the right panels indicate ±1 standard deviation from temporal variability around the period means. Thick lines indicate multi-model median and thin lines indicate individual models in the left panels. Circles are reconstructions of a global climatology for monthly ocean N₂O emissions for the period 1988–2007 by Yang et al. (2020). Note different y-axis scaling compared to Figure 2.

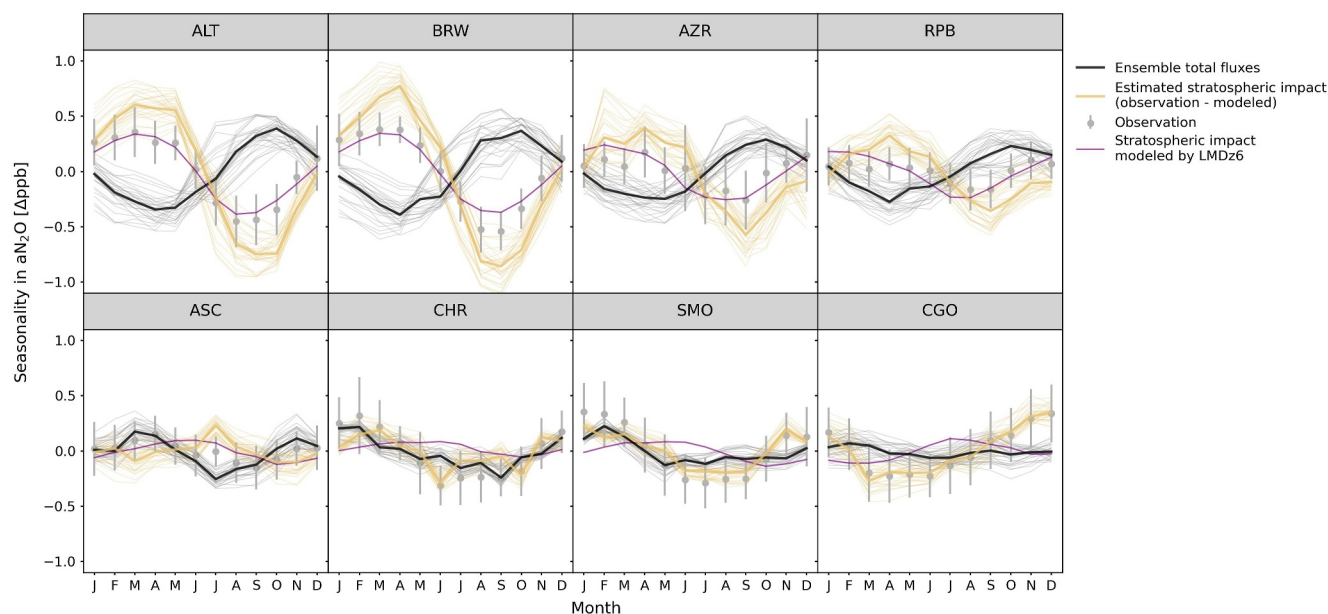


Figure 4. Mismatch (yellow lines) between observed (solid gray circles) and modeled aN_2O seasonality (black lines) at different NOAA/CCGG flask stations (ALT: Alert, BRW: Barrow, AZR: Terceira Island, RPB: Ragged Point, ASC: Ascension Island, CHR: Christmas Island, SMO: Samoa, CGO: Cape Grim) for present day (2001–2020). Thick lines indicate multi-model median and thin lines indicate individual models. Vertical lines on gray circles indicate the standard deviation from temporal variability weighted by measurement uncertainty. The observation-model mismatch (observed—modeled N_2O mixing ratio) provides an estimate of the stratospheric contribution to aN_2O seasonality from N_2O loss and resulting stratosphere-troposphere net fluxes. A modeled stratospheric tracer of N_2O indicating stratospheric contribution for the same period using the chemistry-transport model, LMDz6 (see Ruiz and Prather (2022) for methods), is shown in purple lines for comparison.

et al., 2022; Ruiz & Prather, 2022) and at the sites (Figure 4, purple lines). Moreover, at CGO, the surface flux influence is only 3 months out-of-phase with that of the estimated stratospheric contribution, and the combination of both leads to the observed minimum in May–June.

We demonstrate that surface N_2O emissions contribute substantially to aN_2O seasonality, although the phase of the observed seasonal cycle in the NH mid to high latitudes is out-of-phase with the influence of surface fluxes and tropospheric transport. This is due to the strong impact from stratosphere-troposphere exchanges. The impact of land N_2O emissions on aN_2O seasonality is modeled to have increased considerably (61%, 64%, 49%,

Table 6

Modeled Seasonal Min-To-Max Amplitude of Atmospheric N_2O Mixing Ratio (ppb; Multi-Model Median [25th Percentile, 75th Percentile] Derived From Long-Term Average of Modeled aN_2O Seasonal Cycle) Attributed to Total of Land and Ocean Emissions As Well As Separated and the Mismatch (Estimated Stratospheric Contribution by Observed—Modeled N_2O Mixing Ratio for Present Day) at NOAA/CCGG Stations (ALT: Alert, BRW: Barrow, AZR: Terceira Island, RPB: Ragged Point, CHR: Christmas Island, ASC: Ascension Island, SMO: Samoa, CGO: Cape Grim)

| Site | Present day (2001–2020) | | | | Pre-industrial (1861–1880) | | |
|------|-------------------------|-------------------|-------------------|-------------------|----------------------------|-------------------|-------|
| | Land + ocean | Land | Ocean | Mismatch | Land + ocean | Land | Ocean |
| ALT | 0.70 [0.65, 0.85] | 0.78 [0.71, 0.94] | 0.16 [0.15, 0.18] | 1.47 [1.37, 1.59] | 0.44 [0.38, 0.50] | 0.48 [0.39, 0.56] | 0.14 |
| BRW | 0.77 [0.67, 0.87] | 0.80 [0.72, 0.93] | 0.19 [0.18, 0.22] | 1.74 [1.63, 1.89] | 0.43 [0.36, 0.50] | 0.49 [0.41, 0.57] | 0.17 |
| AZR | 0.60 [0.54, 0.68] | 0.68 [0.62, 0.77] | 0.21 [0.14, 0.28] | 0.69 [0.63, 0.77] | 0.37 [0.34, 0.40] | 0.46 [0.38, 0.48] | 0.17 |
| RPB | 0.58 [0.45, 0.69] | 0.60 [0.51, 0.70] | 0.18 [0.15, 0.20] | 0.81 [0.65, 0.98] | 0.54 [0.41, 0.56] | 0.47 [0.36, 0.48] | 0.20 |
| CHR | 0.47 [0.45, 0.56] | 0.48 [0.42, 0.54] | 0.15 [0.10, 0.20] | 0.58 [0.55, 0.61] | 0.28 [0.26, 0.39] | 0.24 [0.23, 0.32] | 0.09 |
| ASC | 0.47 [0.42, 0.59] | 0.41 [0.37, 0.46] | 0.18 [0.14, 0.22] | 0.63 [0.60, 0.68] | 0.48 [0.40, 0.49] | 0.30 [0.28, 0.37] | 0.26 |
| SMO | 0.39 [0.36, 0.46] | 0.32 [0.27, 0.39] | 0.14 [0.12, 0.17] | 0.83 [0.81, 0.89] | 0.29 [0.21, 0.32] | 0.22 [0.14, 0.27] | 0.14 |
| CGO | 0.28 [0.23, 0.38] | 0.25 [0.21, 0.34] | 0.25 [0.24, 0.29] | 0.89 [0.85, 0.95] | 0.24 [0.20, 0.26] | 0.19 [0.14, 0.26] | 0.24 |

Note. Pre-industrial N_2O fluxes from the ocean are only available for Bern3D.

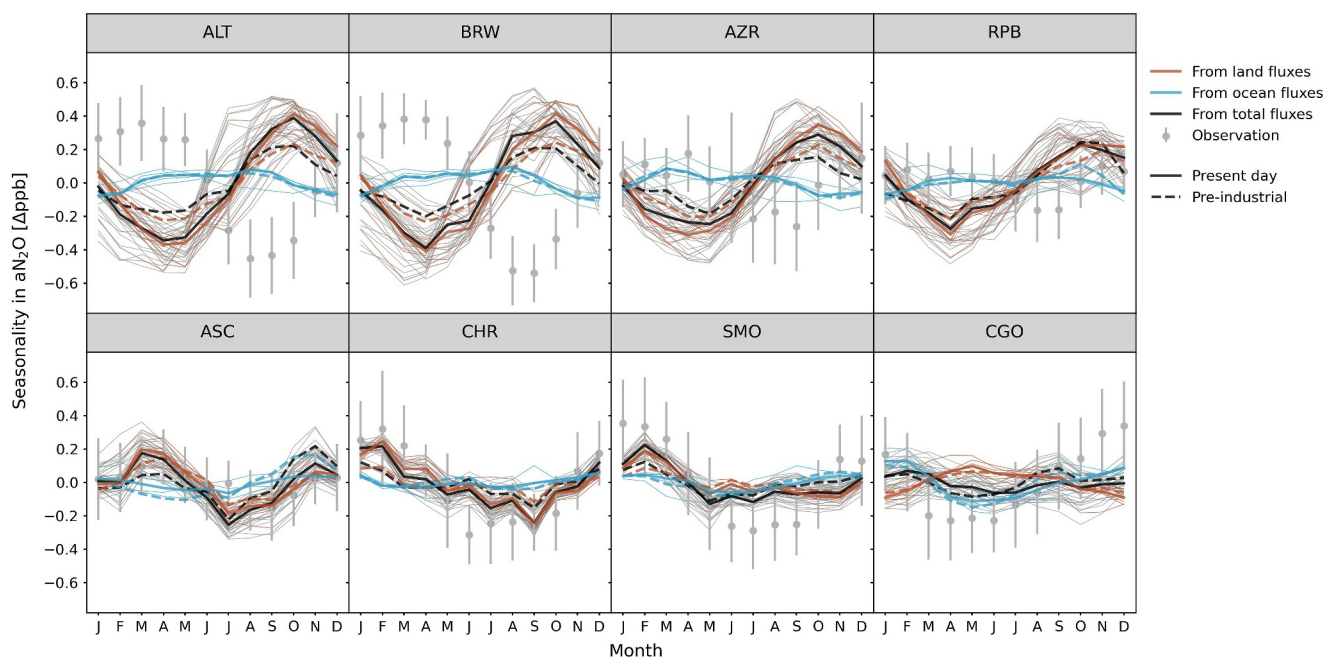


Figure 5. Long-term average seasonality of observed aN_2O (solid gray circles) and modeled aN_2O (lines) at different NOAA/CCGG flask stations (ALT: Alert, BRW: Barrow, AZR: Terceira Island, RPB: Ragged Point, ASC: Ascension Island, CHR: Christmas Island, SMO: Samoa, CGO: Cape Grim). Modeled aN_2O seasonality is attributed to the N_2O emissions from the land (solid red lines) and the ocean (solid blue lines), and total emissions (solid black lines) for present day (2001–2020). Only the multi-model median of aN_2O seasonality for the pre-industrial period (1861–1880) is given (dashed lines). Thick lines indicate multi-model median and thin lines indicate individual models. Vertical lines on gray circles indicate observed temporal variability weighted with measurement uncertainty.

and 26% at ALT, BRW, AZR, and RPB, respectively) over the industrial period (Figure 5; Table 6). Ruiz et al. (2021) suggested that the observed seasonality of aN_2O in the NH is explained by net fluxes from STE rather than surface emissions. However, we show that the influence of surface emissions is an important contribution to the net seasonal cycle, and without it, the seasonal amplitude would be larger by 110% and 126% in the NH high latitudes, while 16% and 39% at mid to low latitudes, all with a later minimum by ~ 1 month (Figure 4; Table 6). With global change and likely increasing N-fertilizer use, terrestrial biosphere N_2O emissions are potentially continuing to increase in the future, thus leading to a more important contribution of these emissions to the seasonal cycle of aN_2O in the years to come. This future increase in the contribution from land N_2O fluxes is possibly lowering the seasonal amplitude and causing a shift in phasing for aN_2O seasonality, especially in high-latitude regions.

We analyzed aN_2O for a relatively small set of eight tropospheric background sites to demonstrate the significant influence of terrestrial N_2O emissions on aN_2O seasonality. The sites are included in the TM2 transport matrix and have long-term aN_2O measurements. These sites are remote from major terrestrial N_2O source areas. Future work may consider more sites for gaining a more complete regional picture. In any case, we expect an even larger role for terrestrial emissions at sites closer to major emission areas than for the remote sites analyzed here. Furthermore, the atmospheric transport matrix of TM2 (Kaminski et al., 1999) used in this work represents a single-year meteorological field and hence cannot account for atmospheric cycles and climate patterns with a non-annual frequency, such as Quasi-Biennial Oscillation and El Niño/La Niña Southern Oscillation, which have substantial impacts especially for low latitude regions (Baldwin et al., 2002; Ray et al., 2020), namely CHR, ASC, and SMO in this study. For example, Ruiz et al. (2021) showed that the modeled Quasi-Biennial Oscillation amplitude can be as large as the annual amplitude in the mid-latitudes, leaving the seasonality less clear than other regions. The effect of interannual variability from all possible causes on aN_2O seasonality is imprinted in measured aN_2O . The observation-inferred seasonal amplitudes show a standard deviation of 21%–36% around the period mean seasonal amplitude for the different stations, and 53%–73% for AZR and CHR where the long-term continuous measurements are limited (Table 3). Thus, climate variability causes a significant year-to-year variability in the seasonal amplitude of aN_2O . Moreover, Thompson et al. (2014) compared a set of chemistry-transport models that consider different annual meteorological fields and showed considerable model

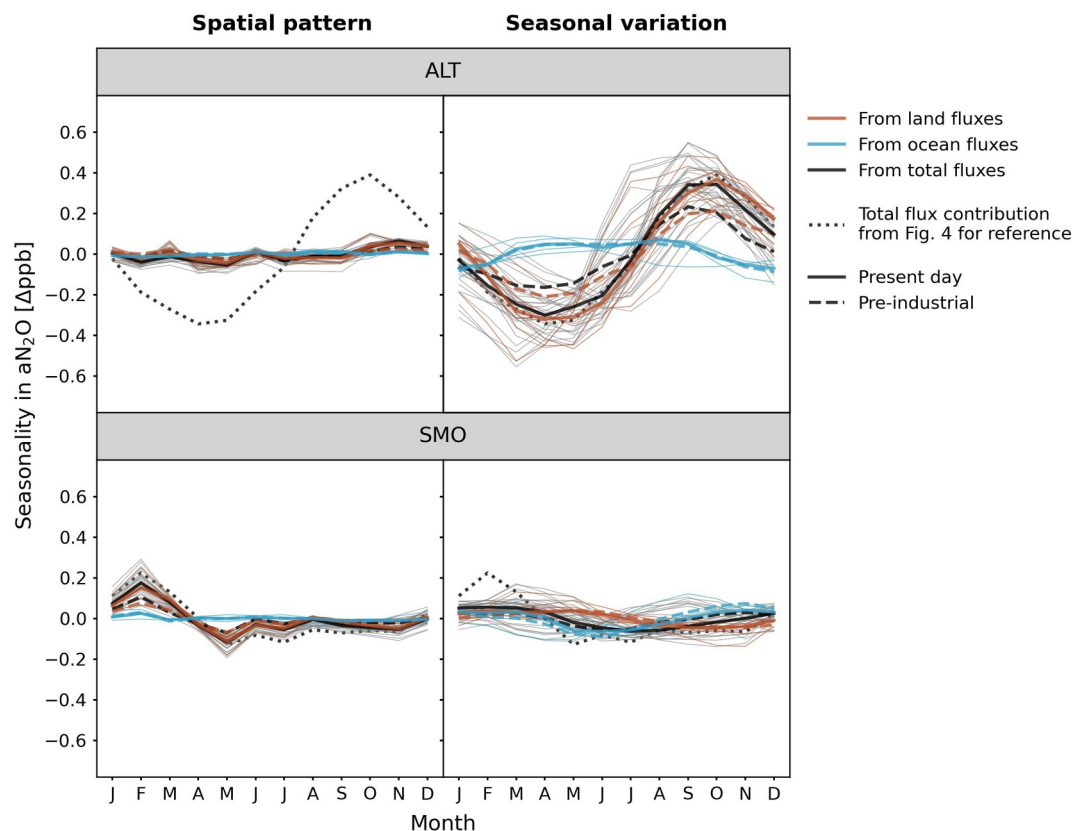


Figure 6. Modeled aN_2O seasonality at different NOAA/CCGG flask stations (ALT: Alert; SMO: Samoa) from spatial pattern (deseasonalized fluxes as 12-month running mean) and seasonal variation (detrended fluxes) of N_2O fluxes for pre-industrial period (1861–1880; dashed lines) and present day (2001–2020; solid lines). Only the multi-model median of aN_2O seasonality for the pre-industrial period (1861–1880) is given (dashed lines). Thick lines indicate multi-model median and thin lines indicate individual models. The aN_2O seasonality modeled from total (including both spatial and seasonal variations) land and ocean N_2O emissions of present day are repeated for reference in all panels.

spread in both phasing and amplitude for modeled aN_2O seasonality. Such differences also exist among models simulating stratosphere-troposphere exchanges for N_2O in the NH and even more so in the SH (Liang et al., 2022; Ruiz et al., 2021). Thus, uncertainties from transport models also impose additional challenges in assessing source contributions to aN_2O variations and in comparing results across studies.

There is a large model spread in N_2O emissions (Figures 1d–1f, Figure S2 in Supporting Information S1) as well as their seasonal amplitudes (the interquartile range is 28%–148% of the multi-model median of land and ocean seasonal amplitude for different latitudinal zones, Figure 2; Table 5). For land emissions, which is the main source of N_2O , important processes of the coupled nitrogen-carbon-water cycles are represented differently among NMIP models (see evaluation of some of the models by Kou-Giesbrecht et al., 2023), contributing to the large model spread in emissions. Further, there are uncertainties in N fertilizer application schemes, for instance, the application timing for synthetic fertilizers as well as the usage of manure fertilizers. The spread in emissions translates to a considerable range in modeled aN_2O seasonal cycle (interquartile range is 21%–52% of the multi-model median for the land contribution to the aN_2O seasonal amplitude, and 17%–42% for the ocean contribution across sites, while the interquartile range in the stratospheric contribution is typically 11% and 15% (except at AZR, 20% and RBP, 42%; Figure 5; Table 6).

Our study suggests that drivers for the seasonality of aN_2O vary by site and land N_2O emissions have become increasingly influential. Our understanding of the N cycle would benefit greatly from further efforts to reduce uncertainties in processes from surface fluxes to atmospheric transport and chemistry. Future research considering observations and models can provide further evidence for the sources and impacts of N_2O emissions.

5. Conclusions and Outlook

Our results demonstrate that surface N₂O fluxes contribute significantly to the seasonality of tropospheric N₂O at different observation sites. The model results from the Nitrogen/N₂O Model Intercomparison Project suggest a strong increase in the seasonal variation of terrestrial biosphere N₂O emissions over the industrial period with an amplifying influence on the seasonality of tropospheric N₂O. The wide range of spatial and temporal variations simulated among NMIP-2 models calls for model improvements and validations on different scales. In situ aN₂O observations, in combination with atmospheric chemistry and transport models, may provide a potential novel top-down constraint for nitrogen-N₂O-enabled land biosphere models that are used to project the land sink of anthropogenic carbon, atmospheric CO₂ and N₂O, and global warming.

Data Availability Statement

The data and scripts for reproducing the figures are available on Zenodo (Sun, 2024).

Acknowledgments

The authors thank Thomas Kaminski for providing the atmospheric transport matrix. This study was supported by the Swiss National Science Foundation (200020 200511). Simulations of LPX-Bern and Bern3D were performed on UBELIX (<https://www.id.unibe.ch/hpc>), the HPC cluster at the University of Bern. Aurich Jeltsch-Thömmes is acknowledged for providing the results of Bern3D. AI was supported by the Environmental Research and Technology Development Fund (JPMEEF21S20830) of the Ministry of the Environment and the Environmental Restoration and Conservation Agency of Japan. QZ acknowledges the support from the U.S. Department of Energy through the Reducing Uncertainties in Biogeochemical Interactions through Synthesis and Computation Scientific Focus Area (RUBISCO SFA) project. HT and NP acknowledge the funding support from the U.S. National Science Foundation (Grant: 1903722). RLT acknowledges funding through the Copernicus Atmosphere Monitoring Service (<https://atmosphere.copernicus.eu/>), implemented by ECMWF on behalf of the European Commission and computing resources provided by LSCE. We thank the NOAA/CCGG for the data from CCGGSurfaceFlask v2.0 ObsPack. The constructive comments from two anonymous reviewers and the editor are highly appreciated. Open access funding provided by Universitat Bern.

References

- Bakker, D. C. E., Bange, H. W., Gruber, N., Johannessen, T., Upstill-Goddard, R. C., Borges, A. V., et al. (2014). Air-sea interactions of natural long-lived greenhouse gases (CO₂, N₂O, CH₄) in a changing climate. In *Ocean-atmosphere interactions of gases and particles* (pp. 113–169). Baldwin, M. P., Gray, L. J., Dunkerton, T. J., Hamilton, K., Haynes, P. H., Randel, W. J., et al. (2002). The quasi-biennial oscillation. *Reviews of Geophysics*, 39(2), 179–229. <https://doi.org/10.1029/1999rg000073>
- Battaglia, G., & Joos, F. (2018). Marine N₂O emissions from nitrification and denitrification constrained by modern observations and projected in multimillennial global warming simulations. *Global Biogeochemical Cycles*, 32(1), 92–121. <https://doi.org/10.1002/2017gb005671>
- Bergamaschi, P., Corazza, M., Karstens, U., Athanassiadou, M., Thompson, R. L., Pison, I., et al. (2015). Top-down estimates of European CH₄ and N₂O emissions based on four different inverse models. *Atmospheric Chemistry and Physics*, 15(2), 715–736. <https://doi.org/10.5194/acp-15-715-2015>
- Bouwman, A. F., & Taylor, J. A. (1996). Testing high-resolution nitrous oxide emission estimates against observations using an atmospheric transport model. *Global Biogeochemical Cycles*, 10(2), 307–318. <https://doi.org/10.1029/96gb00191>
- Breider, F., Yoshikawa, C., Makabe, A., Toyoda, S., Wakita, M., Matsui, Y., et al. (2019). Response of N₂O production rate to ocean acidification in the western North Pacific. *Nature Climate Change*, 9(12), 954–958. <https://doi.org/10.1038/s41558-019-0605-7>
- Butterbach-Bahl, K., Bagges, E. M., Dannenmann, M., Kiese, R., & Zechmeister-Boltenstern, S. (2013). Nitrous oxide emissions from soils: How well do we understand the processes and their controls? *Philosophical Transactions B*, 368(1621), 20130122. <https://doi.org/10.1098/rstb.2013.0122>
- Canadell, J. G., Monteiro, P. M., Costa, M. H., Cotrim da Cunha, L., Cox, P. M., Eliseev, A. V., et al. (2021). Global carbon and other biogeochemical cycles and feedbacks. In V. Masson-Delmotte, P. Zhai, A. Pirani, S. L. Connors, C. Péan, S. Berger, et al. (Eds.), *Climate Change 2021: The Physical Science Basis. Contribution of Working Group I to the Sixth Assessment Report of the Intergovernmental Panel on Climate Change* (pp. 673–816). IPCC. <https://doi.org/10.1017/9781009157896.007>
- Cardenas, L. M., Gooday, R., Brown, L., Scholefield, D., Cuttle, S., Gilhespy, S., et al. (2013). Towards an improved inventory of N₂O from agriculture: Model evaluation of N₂O emission factors and N fraction leached from different sources in UK agriculture. *Atmospheric Environment*, 79, 340–348. <https://doi.org/10.1016/j.atmosenv.2013.06.033>
- Carroll, D., Menemenlis, D., Adkins, J. F., Bowman, K. W., Brix, H., Dutkiewicz, S., et al. (2020). The ECCO-Darwin data-assimilative global ocean biogeochemistry model: Estimates of seasonal to multidecadal surface ocean pCO₂ and air-sea CO₂ flux. *Journal of Advances in Modeling Earth Systems*, 12(10), e2019MS001888. <https://doi.org/10.1029/2019ms001888>
- Crutzen, P. J. (1970). Influence of nitrogen oxides on atmospheric ozone content. *The Quarterly Journal of the Royal Meteorological Society*, 96(408), 320–325. <https://doi.org/10.1002/qj.49709640815>
- Dijkstra, F. A., Prior, S. A., Runion, G. B., Torbert, H. A., Tian, H., Lu, C., & Venterea, R. T. (2012). Effects of elevated carbon dioxide and increased temperature on methane and nitrous oxide fluxes: Evidence from field experiments. *Frontiers in Ecology and the Environment*, 10(10), 520–527. <https://doi.org/10.1890/120059>
- Dlugokencky, E., Petron, G., Crotwell, A., Higgs, J., Vaughn, B., Michel, S., et al. (2021). *Measurements of CO₂, CH₄, CO, N₂O, H₂, SF₆ and isotopic ratios in flask-air samples at global and regional background sites starting in 1967*. G. M. L. NOAA Earth System Research Laboratories.
- Feigenwinter, I., Hörtnagl, L., & Buchmann, N. (2023). N₂O and CH₄ fluxes from intensively managed grassland: The importance of biological and environmental drivers vs. management. *Science of the Total Environment*, 903, 166389. <https://doi.org/10.1016/j.scitotenv.2023.166389>
- Fischer, H., Schmitt, J., Bock, M., Seth, B., Joos, F., Spahni, R., et al. (2019). N₂O changes from the Last Glacial Maximum to the preindustrial—Part 1: Quantitative reconstruction of terrestrial and marine emissions using N₂O stable isotopes in ice cores. *Biogeosciences*, 16(20), 3997–4021. <https://doi.org/10.5194/bg-16-3997-2019>
- Forster, P., Storelvmo, T., Armour, K., Collins, W., Dufresne, J.-L., Frame, D., et al. (2021). In V. Masson-Delmotte, P. Zhai, A. Pirani, S. L. Connors, C. Péan, S. Berger, et al. (Eds.), *The Earth's energy budget, climate feedbacks, and climate sensitivity* Rep. Cambridge University Press.
- Fuchs, K., Merbold, L., Buchmann, N., Bellocchi, G., Bindi, M., Brilli, L., et al. (2020). Evaluating the potential of legumes to mitigate N₂O emissions from permanent grassland using process-based models. *Global Biogeochemical Cycles*, 34(12). <https://doi.org/10.1029/2020gb006561>
- Ganesan, A. L., Manizza, M., Morgan, E. J., Harth, C. M., Kozlova, E., Lueker, T., et al. (2020). Marine nitrous oxide emissions from three eastern boundary upwelling systems inferred from atmospheric observations. *Geophysical Research Letters*, 47(14), e2020GL087822. <https://doi.org/10.1029/2020gl087822>
- Harris, I. C. (2021). In N. E. C. f. E. D. Analysis (Ed.), *CRU JRA v2.2: A forcings dataset of gridded land surface blend of Climatic Research Unit (CRU) and Japanese reanalysis (JRA) data; Jan.1901–Dec.2020*. University of East Anglia Climatic Research Unit.

- Hegglin, M., Kinnison, D., & Lamarque, J.-F. (2016). *CCMI nitrogen surface fluxes in support of CMIP6—version 2.0*. Earth System Grid Federation.
- Heimann, M. (1995). The global atmospheric tracer model TM2 Rep.
- Hirsch, A. I., Michalak, A. M., Bruhwiler, L. M., Peters, W., Dlugokencky, E. J., & Tans, P. P. (2006). Inverse modeling estimates of the global nitrous oxide surface flux from 1998–2001. *Global Biogeochemical Cycles*, 20(1). <https://doi.org/10.1029/2004gb002443>
- Hoyer, S., & Hamman, J. (2017). xarray: Labeled arrays and datasets in Python [Software]. *Journal of Open Research Software*, 5(1), 10. <https://doi.org/10.5334/jors.148>
- Hunter, J. D. (2007). Matplotlib: A 2D graphics environment. *Computing in Science and Engineering*, 9(3), 90–95. <https://doi.org/10.1109/mcse.2007.55>
- Hurt, G. C., Chini, L., Sahajpal, R., Frolking, S., Bodirsky, B. L., Calvin, K., et al. (2020). Harmonization of global land use change and management for the period 850–2100 (LUH2) for CMIP6. *Geoscientific Model Development*, 13(11), 5425–5464. <https://doi.org/10.5194/gmd-13-5425-2020>
- Hutchins, D. A., & Capone, D. C. (2022). The marine nitrogen cycle: New developments and global change. *Nature Reviews Microbiology*, 20(7), 401–414. <https://doi.org/10.1038/s41579-022-00687-z>
- IPCC. (2021). In V. Masson-Delmotte, P. Zhai, A. Pirani, S. L. Connors, C. Péan, S. Berger, et al. (Eds.), *Climate Change 2021: The Physical Science Basis. Contribution of Working Group I to the Sixth Assessment Report of the Intergovernmental Panel on Climate Change Rep.* Cambridge University Press. <https://doi.org/10.1017/9781009157896>
- IPCC. (2022). In H.-O. Pörtner, D. C. Roberts, M. Tignor, E. S. Poloczanska, K. Mintenbeck, A. Alegría, et al. (Eds.), *Climate change 2022: Impacts, adaptation, and vulnerability. Contribution of Working Group II to the Sixth Assessment Report of the Intergovernmental Panel on Climate Change* (p. 3056). Cambridge University Press. <https://doi.org/10.1017/9781009325844>
- Ito, A., Nishina, K., Ishijima, K., Hashimoto, S., & Inatomi, M. (2018). Emissions of nitrous oxide (N₂O) from soil surfaces and their historical changes in East Asia: A model-based assessment. *Progress in Earth and Planetary Science*, 5(55), 55. <https://doi.org/10.1186/s40645-40018-40215-40644>
- James, P., Stohl, A., Forster, C., Eckhardt, S., Seibert, P., & Frank, A. (2003). A 15-year climatology of stratosphere-troposphere exchange with a Lagrangian particle dispersion model—2. Mean climate and seasonal variability. *Journal of Geophysical Research*, 108(D12). <https://doi.org/10.1029/2002jd002639>
- Jiang, X., Ku, W. L., Shia, R.-L., Li, Q., Elkins, J. W., Prinn, R. G., & Yung, Y. L. (2007). Seasonal cycle of N₂O: Analysis of data. *Global Biogeochemical Cycles*, 21(1). <https://doi.org/10.1029/2006gb002691>
- Joos, F., & Spahni, R. (2008). Rates of change in natural and anthropogenic radiative forcing over the past 20,000 years. *Proceedings of the National Academy of Sciences of the United States of America*, 105(5), 1425–1430. <https://doi.org/10.1073/pnas.0707386105>
- Joos, F., Spahni, R., Stocker, B. D., Lienert, S., Müller, J., Fischer, H., et al. (2020). N₂O changes from the last glacial maximum to the preindustrial—Part 2: Terrestrial N₂O emissions and carbon-nitrogen cycle interactions. *Biogeosciences*, 17(13), 3511–3543. <https://doi.org/10.5194/bg-17-3511-2020>
- Kaminski, T., Heimann, M., & Giering, R. (1999). A coarse grid three-dimensional global inverse model of the atmospheric transport—1. Adjoint model and Jacobian matrix. *Journal of Geophysical Research*, 104(D15), 18535–18553. <https://doi.org/10.1029/1999jd900147>
- Kock, A., & Bange, H. W. (2015). Counting the ocean's greenhouse gas emissions. *Eos*, 96(3), 10–13. <https://doi.org/10.1029/2015eo023665>
- Kou-Giesbrecht, S., Arora, V. K., Seiler, C., Arneeth, A., Falk, S., Jain, A. K., et al. (2023). Evaluating nitrogen cycling in terrestrial biosphere models: A disconnect between the carbon and nitrogen cycles. *Earth System Dynamics*, 14(4), 767–795. <https://doi.org/10.5194/esd-14-767-2023>
- Lan, X., Tans, P., & Thoning, K. W. (2023). Trends in globally-averaged CO₂ determined from NOAA global monitoring laboratory measurements. Version 2023-03 NOAA/GML. <https://gml.noaa.gov/ccgg/trends/>
- Lan, X., Thoning, K. W., & Dlugokencky, E. J. (2023). Trends in globally-averaged CH₄, N₂O, and SF₆ determined from NOAA global monitoring laboratory measurements [Dataset]. Version 2023-03. <https://doi.org/10.15138/P8XG-AA10>
- Landolfi, A., Somes, C. J., Koeve, W., Zamora, L. M., & Oschlies, A. (2017). Oceanic nitrogen cycling and N₂O flux perturbations in the anthropocene. *Global Biogeochemical Cycles*, 31(8), 1236–1255. <https://doi.org/10.1002/2017gb005633>
- Liang, Q., Nevison, C., Dlugokencky, E., Hall, B. D., & Dutton, G. (2022). 3-D atmospheric modeling of the global budget of N₂O and its isotopologues for 1980–2019: The impact of anthropogenic emissions. *Global Biogeochemical Cycles*, 36(7). <https://doi.org/10.1029/2021gb007202>
- Lienert, S., & Joos, F. (2018). A Bayesian ensemble data assimilation to constrain model parameters and land-use carbon emissions. *Biogeosciences*, 15(9), 2909–2930. <https://doi.org/10.5194/bg-15-2909-2018>
- Ma, M. N., Song, C. Q., Fang, H. J., Zhang, J. B., Wei, J., Liu, S. R., et al. (2022). Development of a process-based N₂O emission model for natural forest and grassland ecosystems. *Journal of Advances in Modeling Earth Systems*, 14(3). <https://doi.org/10.1029/2021ms002460>
- MacFarling Meure, C., Etheridge, D., Trudinger, C., Steele, P., Langenfelds, R., van Ommen, T., et al. (2006). Law Dome CO₂, CH₄ and N₂O ice core records extended to 2000 years BP. *Geophysical Research Letters*, 33(14). <https://doi.org/10.1029/2006gl026152>
- Maier, R., Hörtnagl, L., & Buchmann, N. (2022). Greenhouse gas fluxes (CO₂, N₂O and CH₄) of pea and maize during two cropping seasons: Drivers, budgets, and emission factors for nitrous oxide. *Science of the Total Environment*, 849, 157541. <https://doi.org/10.1016/j.scitotenv.2022.157541>
- Manizza, M., Keeling, R. F., & Nevison, C. D. (2012). On the processes controlling the seasonal cycles of the air-sea fluxes of O-2 and N₂O: A modelling study. *Tellus B: Chemical and Physical Meteorology*, 64(1), 18429. <https://doi.org/10.3402/tellusb.v64i0.18429>
- Martins, M. D., Necpalova, M., Ammann, C., Buchmann, N., Calanca, P., Flechard, C. R., et al. (2022). Modeling N₂O emissions of complex cropland management in Western Europe using DayCent: Performance and scope for improvement. *European Journal of Agronomy*, 141, 126613. <https://doi.org/10.1016/j.eja.2022.126613>
- Melton, J. R., Arora, V. K., Wisemig-Cojoc, E., Seiler, C., Fortier, M., Chan, E., & Teckentrup, L. (2020). CLASSIC v1.0: The open-source community successor to the Canadian Land Surface Scheme (CLASS) and the Canadian Terrestrial Ecosystem Model (CTEM)—Part 1: Model framework and site-level performance. *Geoscientific Model Development*, 13(6), 2825–2850. <https://doi.org/10.5194/gmd-13-2825-2020>
- Merbold, L., Eugster, W., Stieger, J., Zahniser, M., Nelson, D., & Buchmann, N. (2014). Greenhouse gas budget (CO₂, CH₄ and N₂O) of intensively managed grassland following restoration. *Global Change Biology*, 20(6), 1913–1928. <https://doi.org/10.1111/gcb.12518>
- Mueller, R. (2021). The impact of the rise in atmospheric nitrous oxide on stratospheric ozone This article belongs to Ambio's 50th Anniversary Collection. *Ambio*, 50(1), 35–39. Theme: Ozone Layer. <https://doi.org/10.1007/s13280-020-01428-3>

- Nevison, C. D., Dlugokencky, E., Dutton, G., Elkins, J. W., Fraser, P., Hall, B., et al. (2011). Exploring causes of interannual variability in the seasonal cycles of tropospheric nitrous oxide. *Atmospheric Chemistry and Physics*, 11(8), 3713–3730. <https://doi.org/10.5194/acp-11-3713-2011>
- Nevison, C. D., Keeling, R. F., Weiss, R. F., Popp, B. N., Jin, X., Fraser, P. J., et al. (2005). Southern Ocean ventilation inferred from seasonal cycles of atmospheric N₂O and O₂/N₂ at Cape Grim, Tasmania. *Tellus B: Chemical and Physical Meteorology*, 57(3), 218–229. <https://doi.org/10.1111/j.1600-0889.2005.00143.x>
- Park, S., Croteau, P., Boering, K. A., Etheridge, D. M., Ferretti, D., Fraser, P. J., et al. (2012). Trends and seasonal cycles in the isotopic composition of nitrous oxide since 1940. *Nature Geoscience*, 5(4), 261–265. <https://doi.org/10.1038/ngeo1421>
- Pastorello, G., Trotta, C., Canfora, E., Chu, H., Christianson, D., Cheah, Y. W., et al. (2020). The FLUXNET2015 dataset and the ONEFlux processing pipeline for eddy covariance data. *Scientific Data*, 7(1), 225. <https://doi.org/10.1038/s41597-020-0534-3>
- Patra, P. K., Dlugokencky, E. J., Elkins, J. W., Dutton, G. S., Tohjima, Y., Sasakawa, M., et al. (2022). Forward and inverse modeling of atmospheric nitrous oxide using MIROC4-atmospheric chemistry-transport model. *Journal of the Meteorological Society of Japan Series II*, 100(2), 361–386. <https://doi.org/10.2151/jmsj.2022-018>
- Petitjean, C., Henault, C., Perrin, A. S., Pontet, C., Metay, A., Bernoux, M., et al. (2015). Soil N₂O emissions in French Guiana after the conversion of tropical forest to agriculture with the chop-and-mulch method. *Agriculture, Ecosystems & Environment*, 208, 64–74. <https://doi.org/10.1016/j.agee.2015.04.004>
- Prather, M. J., Hsu, J., DeLuca, N. M., Jackman, C. H., Oman, L. D., Douglass, A. R., et al. (2015). Measuring and modeling the lifetime of nitrous oxide including its variability. *Journal of Geophysical Research: Atmospheres*, 120(11), 5693–5705. <https://doi.org/10.1002/2015jd023267>
- Ravishankara, A. R., Daniel, J. S., & Portmann, R. W. (2009). Nitrous oxide (N₂O): The dominant ozone-depleting substance emitted in the 21st century. *Science*, 326(5949), 123–125. <https://doi.org/10.1126/science.1176985>
- Ray, E. A., Portmann, R. W., Yu, P., Daniel, J., Montzka, S. A., Dutton, G. S., et al. (2020). The influence of the stratospheric Quasi-Biennial Oscillation on trace gas levels at the Earth's surface. *Nature Geoscience*, 13(1), 22–27. <https://doi.org/10.1038/s41561-019-0507-3>
- Rubino, M., Etheridge, D. M., Thornton, D. P., Howden, R., Allison, C. E., Francey, R. J., et al. (2019). Revised records of atmospheric trace gases CO₂, CH₄, N₂O, and delta C-13-CO₂ over the last 2000 years from Law Dome, Antarctica. *Earth System Science Data*, 11(2), 473–492. <https://doi.org/10.5194/essd-11-473-2019>
- Ruiz, D. J., & Prather, M. J. (2022). From the middle stratosphere to the surface, using nitrous oxide to constrain the stratosphere–troposphere exchange of ozone. *Atmospheric Chemistry and Physics*, 22(3), 2079–2093. <https://doi.org/10.5194/acp-22-2079-2022>
- Ruiz, D. J., Prather, M. J., Strahan, S. E., Thompson, R. L., Froidevaux, L., & Steenrod, S. D. (2021). How atmospheric chemistry and transport drive surface variability of N₂O and CFC-11. *Journal of Geophysical Research: Atmospheres*, 126(8). <https://doi.org/10.1029/2020jd033979>
- Schilt, A., Baumgartner, M., Blunier, T., Schwander, J., Spahni, R., Fischer, H., & Stocker, T. F. (2010). Glacial-interglacial and millennial-scale variations in the atmospheric nitrous oxide concentration during the last 800,000 years. *Quaternary Science Reviews*, 29(1–2), 182–192. <https://doi.org/10.1016/j.quascirev.2009.03.011>
- Séférian, R., Nabat, P., Michou, M., Saint-Martin, D., Voldoire, A., Colin, J., et al. (2019). Evaluation of CNRM Earth system model, CNRM-ESM2-1: Role of Earth system processes in present-day and future climate. *Journal of Advances in Modeling Earth Systems*, 11(12), 4182–4227. <https://doi.org/10.1029/2019ms001791>
- Sun, Q. (2024). Data and scripts for figures for "The modeled seasonal cycles of land biosphere and ocean N₂O fluxes and atmospheric N₂O [Dataset]. *Zenodo*. <https://doi.org/10.5281/zenodo.10849772>
- Shu, S. J., Jain, A. K., Koven, C. D., & Mishra, U. (2020). Estimation of permafrost SOC stock and turnover time using a land surface model with vertical heterogeneity of permafrost soils. *Global Biogeochemical Cycles*, 34(11). <https://doi.org/10.1029/2020gb006585>
- The pandas development team. (2020). pandas-dev/pandas: Pandas [Software]. *Zenodo*. <https://doi.org/10.5281/zenodo.3509134>
- Thompson, R. L., Lassaletta, L., Patra, P. K., Wilson, C., Wells, K. C., Gressent, A., et al. (2019). Acceleration of global N₂O emissions seen from two decades of atmospheric inversion. *Nature Climate Change*, 9(12), 993–998. <https://doi.org/10.1038/s41558-019-0613-7>
- Thompson, R. L., Patra, P. K., Ishijima, K., Saikawa, E., Corazza, M., Karstens, U., et al. (2014). TransCom N₂O model inter-comparison—Part 1: Assessing the influence of transport and surface fluxes on tropospheric N₂O variability. *Atmospheric Chemistry and Physics*, 14(8), 4349–4368. <https://doi.org/10.5194/acp-14-4349-2014>
- Tian, H., Bian, Z., Shi, H., Qin, X., Pan, N., Lu, C., et al. (2022). History of anthropogenic nitrogen inputs (HaNi) to the terrestrial biosphere: A 5 arcmin resolution annual dataset from 1860 to 2019. *Earth System Science Data*, 14(10), 4551–4568. <https://doi.org/10.5194/essd-14-4551-2022>
- Tian, H., Pan, N., Thompson, R. L., Canadell, J. G., Suntharalingam, P., Regnier, P., et al. (2023). Global nitrous oxide budget 1980–2020. *Earth System Science Data Discussions*, 2023, 1–98.
- Tian, H., Xu, R., Canadell, J. G., Thompson, R. L., Winiwarter, W., Suntharalingam, P., et al. (2020). A comprehensive quantification of global nitrous oxide sources and sinks. *Nature*, 586(7828), 248–256. <https://doi.org/10.1038/s41586-020-2780-0>
- Tian, H., Yang, J., Lu, C., Xu, R., Canadell, J. G., Jackson, R. B., et al. (2018). The global N₂O model Intercomparison project. *Bulletin American Meteorology Society*, 99(6), 1231–1252. <https://doi.org/10.1175/bams-d-17-0212.1>
- Tian, H., Yang, J., Xu, R., Lu, C., Canadell, J. G., Davidson, E. A., et al. (2019). Global soil nitrous oxide emissions since the preindustrial era estimated by an ensemble of terrestrial biosphere models: Magnitude, attribution, and uncertainty. *Global Change Biology*, 25(2), 640–659. <https://doi.org/10.1111/gcb.14514>
- Tian, H. Q., Chen, G., Lu, C., Xu, X., Ren, W., Zhang, B., et al. (2015). Global methane and nitrous oxide emissions from terrestrial ecosystems due to multiple environmental changes. *Ecosystem Health and Sustainability*, 1(1), 1–20. <https://doi.org/10.1890/ehs14-0015.1>
- Van Rossum, G., & Drake, F. L., Jr. (1995). Python tutorial [Software]. *Centrum voor Wiskunde en Informatica Amsterdam, The Netherlands*. <https://dl.acm.org/doi/10.5555/869378>
- Vuichard, N., Messina, P., Luyssaert, S., Guenet, B., Zaehle, S., Ghattas, J., et al. (2019). Accounting for carbon and nitrogen interactions in the global terrestrial ecosystem model ORCHIDEE (trunk version, rev 4999): Multi-scale evaluation of gross primary production. *Geoscientific Model Development*, 12(11), 4751–4779. <https://doi.org/10.5194/gmd-12-4751-2019>
- Walker, A. P., De Kauwe, M. G., Bastos, A., Belmecheri, S., Georgiou, K., Keeling, R. F., et al. (2021). Integrating the evidence for a terrestrial carbon sink caused by increasing atmospheric CO₂. *New Phytologist*, 229(5), 2413–2445. <https://doi.org/10.1111/nph.16866>
- Xu-Ri, & Prentice, I. C. (2008). Terrestrial nitrogen cycle simulation with a dynamic global vegetation model. *Global Change Biology*, 14(8), 1745–1764. <https://doi.org/10.1111/j.1365-2486.2008.01625.x>
- Yang, S., Chang, B. X., Warner, M. J., Weber, T. S., Bourbonnais, A. M., Santoro, A. E., et al. (2020). Global reconstruction reduces the uncertainty of oceanic nitrous oxide emissions and reveals a vigorous seasonal cycle. *Proceedings of the National Academy of Sciences of the United States of America*, 117(22), 11954–11960. <https://doi.org/10.1073/pnas.1921914117>

- Yu, L., Harris, E., Henne, S., Eggleston, S., Steinbacher, M., Emmenegger, L., et al. (2020). The isotopic composition of atmospheric nitrous oxide observed at the high-altitude research station Jungfraujoch, Switzerland. *Atmospheric Chemistry and Physics*, *20*(11), 6495–6519. <https://doi.org/10.5194/acp-20-6495-2020>
- Zaehle, S., & Friend, A. D. (2010). Carbon and nitrogen cycle dynamics in the O-CN land surface model: 1. Model description, site-scale evaluation, and sensitivity to parameter estimates. *Global Biogeochemical Cycles*, *24*. <https://doi.org/10.1029/2009gb003521>
- Zhu, Q., Riley, W. J., Tang, J. Y., Collier, N., Hoffman, F. M., Yang, X. J., & Bisht, G. (2019). Representing nitrogen, phosphorus, and carbon interactions in the E3SM land model: Development and global benchmarking. *Journal of Advances in Modeling Earth Systems*, *11*(7), 2238–2258. <https://doi.org/10.1029/2018ms001571>